Multimodal Neuroimaging (fMRI and fNIRS) at WPI

PracticePoint

Data Processing in Functional Near-Infrared Spectroscopy (fNIRS) Steady State Research for Future Collation with fMRI Data.

Submitted by:

Milad Jaffari

Stuart Elmhurst

Vishali Baker

Fatimah Daffaie

Amanda Shea

Christopher Davis

Table of Contents

Table of Figures

Abstract

Resting-state functional connectivity (RSFC) is a measure of temporal correlation in the absence of an event or stimuli. The most common technique to analyze these networks is through functional magnetic resonance imaging (fMRI). While this method provides reliable, insightful data, it has inherent limitations. In recent studies, however, data suggests that an alternative modality referred to as functional near-infrared spectroscopy (fNIRS) may offer a unique opportunity to investigate brain functionality and whole brain connectivity by proxy. This study analyzes cortical neural hemodynamics during resting-state using fNIRS for future collation with fMRI data and applications in whole brain RSFC research. For analysis, a sample set of seven participating healthy individuals over age 18 underwent multimodal neuroimaging utilizing both fMRI and fNIRS imaging techniques simultaneously. This data was processed in nirsLAB software using a generalized linear model (GLM) analysis to derive the areas of the cortex that experienced significant increases in hemoglobin. The results of this study did find spontaneous increases in hemoglobin in the four valid samples analyzed, as expected with resting-state data. However, the overall consensus was that the sample set experienced a substantial loss of data integrity across the 20 channels observed for each subject.

1. Background/Introduction

The significant correlation of spontaneous neural activity between functionally related, spatially remote regions of the brain is referred to as resting-state functional connectivity (RSFC). In other words, if two regions are considered to show functional connectivity, then there exists a statistical relationship between their respective measures of neural activity. Resting-state networks help to provide information on intrinsic functionalities of the brain, independent of stimulus or event-biased responses. Thus far, there have been relatively few non-invasive neuroimaging technologies utilized to study RSFC, with the primary modalities being functional magnetic resonance imaging (fMRI) and positron emission tomography (PET) (Plichta, 2006). Advancements in neuroimaging techniques have allowed for the progression of research in understanding brain functionality for healthy brain archetypes as well as neurological or psychiatric conditions. Despite this, it remains a challenge to evaluate how strictly controlled, event-based cognitive tasks relate to everyday brain activity. This is due, in part, to the inherent operating constraints of current standard neuroimaging technologies themselves. Notably, a promising and relatively new neuroimaging modality, functional near-infrared spectroscopy (fNIRS), is currently being considered a potential solution to overcoming these restrictions (Plichta, 2006).

fNIRS is an optical, non-invasive hemodynamic neuroimaging technique that indirectly measures neural activity in the brain's cortex via neurovascular coupling. This method works by quantifying changes in cortical hemoglobin concentrations using optical intensity measurements. These measurements are derived from a series of optodes which are placed on the scalp in a predetermined layout. Optodes are classified as either sources (emitters) or detectors (receivers) depending on their respective function. Sources, which emit NIR light (650-950 nm), can be

either LED-based or infrared laser-based. LED sources emit a Gaussian distribution of wavelengths whereas a laser only has a single wavelength. The NIR light emitted from a source is propagated through the cortex of the brain, up to a few centimeters in depth. Thereafter, the emitted light is attenuated via scattering and absorption into the hemoglobin (and other surrounding tissues). An optode (detector) placed near the source would then be able to collect the backscattered light and measure the optical absorption. Pairing a source and optode detector together provides a standard fNIRS channel that measures the local region response between the source and detector. Specifically, the channel exists within the section of tissue propagated by NIR light and is located at the midpoint between the source and detector, at the depth of the midpoint-to-sensor distance. The measurements taken by the channels rely upon the light absorption spectrum of the hemoglobin in that region. Based on the state of saturation, hemoglobin can exist in its oxygenated (i.e., oxyhemoglobin, HbO2) or deoxygenated (i.e., deoxyhemoglobin, HbR) form. Furthermore, oxyhemoglobin and deoxyhemoglobin absorb NIR light differently. The oxyhemoglobin absorption coefficient is higher for wavelengths greater than 800 nm whereas the deoxyhemoglobin absorption coefficient is higher for wavelengths less than 800 nm. Because oxygenated and deoxygenated hemoglobin have different absorption spectrums, their respective concentrations in various brain regions can be measured and quantified over time.

A crucial consideration in the collection of fNIRS data from these channels is the layout of the optodes themselves. In addition to light detection, the positioning and quantity of probes has a significant impact on the brain region of interest as well as the parameters of the data collection. The design of the optode map layout is, therefore, integral in ensuring the data quality for fNIRS experimentation. Here, the distance between a source and a detector pair, determines

the sensitivity and depth of light penetration into the cortex. Moreover, the number of optodes utilized determines the density of the layout and can affect the accuracy of the data. When designing an optode layout, the region of interest being studied in the brain should be considered, as the optode position determines what regions are observed, as illustrated by Figure 1.

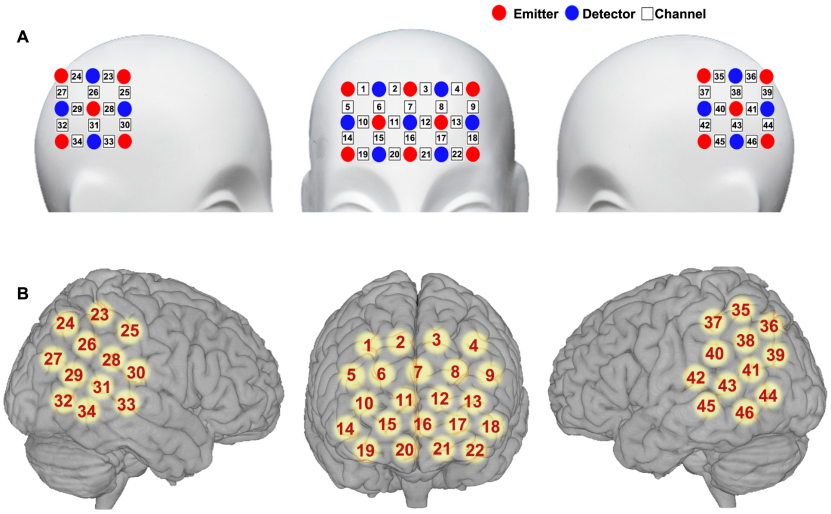

Figure 1: Examples of optode layout affecting brain regions being studied

Through computational analysis, the fNIRS data obtained by channels can be used to generate neural hemodynamic maps showing the levels of oxygenated hemoglobin throughout the observed cortical regions. In the brain, increased blood flow and tissue oxygenation correlate with increased neural activity. When brain region(s) becomes active during an event (such as a task) or induced stimuli, the brain's metabolic demand for oxygen and glucose increases, leading to an increase in blood flow to the corresponding region(s). Because of this, hemodynamic maps are often used to make inferences on what regions display neural activity during an event/stimulus. Comparatively, resting-state fNIRS measures spontaneous hemodynamic fluctuations in the cortex of the brain in the absence of an event or stimuli. This technique is reliable and reproducible in characterizing the brain functional connectivity network while in a spontaneous state. Notably, these maps cannot be utilized to imply causation as the relationship

between neural activity and blood oxygen concentrations is entirely correlative. Numerous physiological variables and couplings interplay with increases and decreases in oxyhemoglobin. These factors inherently limit the ability to analyze event-related brain function based on hemodynamic functional neuroimaging alone and should be considered when interpreting fNIRS data. Moreover, while neural hemodynamic maps are useful for observing regional brain activity individually, they do not provide insight into connectivity.

As previously aforementioned, RSFC is highly useful in providing information on the dynamic coordination of brain activity between disparate neural populations during resting-state. For fNIRS applications, these networks are typically analyzed using 2D functional connectivity matrices as seen in Figure 2. Matrices evaluate connectivity by comparing the similarities in activity between two individual nodes. The more frequently nodes exhibit coactivity, the greater the correlation between the two nodes. Connectivity matrices can be created for oxygenated, deoxygenated, and total hemoglobin levels.

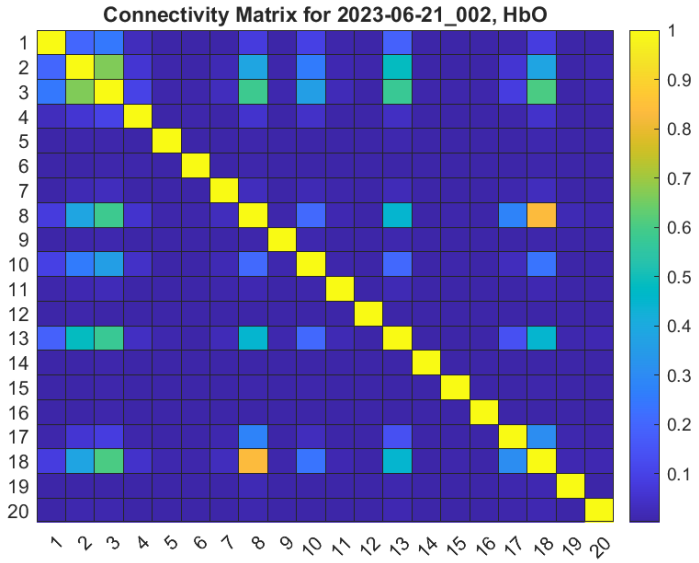

Figure 2: The connectivity matrix created for HbO levels for sample 2023-06-21_002

While fNIRS is able to assess RSFC with many practical advantages, it remains ancillary to other neuroimaging modalities. Currently, fMRI is considered the gold standard non-invasive hemodynamic-based neuroimaging technology and is the most common method used to assess RSFC. The operating principles of magnetic resonance imaging (MRI) are based on the theory of nuclear magnetic resonance which states that all atomic nuclei possess an inherent magnetic moment. Within a magnetic field, such as the one created by an MRI machine, hydrogen nuclei align parallel to the field and rotate at a frequency proportional to the strength of the field. Introducing radiofrequency pulses causes these nuclei to be displaced from their equilibrium state, resulting in a net transverse magnetization vector. After a pulse, the return of these nuclei to equilibrium generates an electromagnetic signal that is differentiable between various tissue types in the body. This signal can be measured within each voxel, which allows for both high spatial resolution and the resulting highly detailed three-dimensional anatomical images characteristic of MRI technology.

fMRI differs from MRI in that it creates a dynamic record of metabolic activities (brain function) over time by measuring the blood-oxygen-level-dependent (BOLD) signal. Here, the BOLD contrast is derived from the differential between the magnetic susceptibility of deoxygenated and oxygenated blood in the brain. Deoxygenated blood is paramagnetic and, therefore, attracted to the magnetic field whereas oxygenated blood is diamagnetic and repels the field. The resulting scans show a high-resolution three-dimensional image of whole brain neural activity. This modality has been favored in neuroimaging because of its high spatial resolution capabilities and its properties as non-invasive, repeatable, and widely available. However, neuroimaging technology is increasingly being applied during more dynamic behaviors in addition to populations that deviate from normative cognition. As such, several limitations

inhibit its practicality in this emerging field of study. Most notably, implicit constraints limit the ecological validity of tasks performed during an MRI scan. Absolute contraindications, such as the presence of metal within the body, pose significant risks during MRI procedures and generally preclude certain individuals from safely undergoing imaging. Separately, relative contraindications such as claustrophobia, movement restrictions, and certain specific retained surgical instruments (such as artery stents and intrauterine devices) pose risks to conducting the procedure that may make this modality inadvisable. Because of limitations such as these, fNIRS offers a more compelling alternative to fMRI, as it can provide brain activity data to researchers and clinicians with greater portability, patient comfort, cost-effectiveness, and improvement in computer interface technology.

When comparing the two neuroimaging modalities, it becomes apparent that while fMRI has its advantages, such as high spatial resolution and whole brain measurement capabilities, it also comes with certain limitations. In this sense, fNIRS addresses some of the shortcomings of fMRI by providing practicality while maintaining neural metrics that are, to an extent, comparable to those achieved with fMRI. Both fNIRS and fMRI neuroimaging modalities share similar hemodynamic origins, making fNIRS an optimal proxy for fMRI. As opposed to an fMRI, which would measure oxygen concentration changes based on the paramagnetic properties of hemoglobin, fNIRS utilizes the different absorption properties of biological chromophores and detects these light changes from anywhere between 700 and 900 nanometers. In particular, this means fMRI can only measure the oxygen-dependent signal whereas fNIRS can separately measure oxygenated, deoxygenated, and total hemoglobin. This can be advantageous in measuring brain activity and hemodynamics as clinicians better understand the involvement of

neural activity and mapping brain activity in clinical settings. As a modality alternative, fNIRS largest advantage over fMRI manifests in regards to practically. This is especially

The multiple contraindications for fMRI can complicate the scanning procedure, limit the population viable to undergo scanning, and restrict data collection feasibility. For example, fMRI requires a person to sit still for up to 60 minutes to be completed successfully, which can be challenging for young patients or patients experiencing chronic pain. For patients, the scan involves compact spaces, loud machine operating noises, and, in some cases, the intravenous injection of contrast dye. Patients with implants containing ferromagnetic metals, such as pacemakers, cannot be scanned due to the strong magnetic fields. Naturally, some patients experience increased levels of stress and anxiety and require sedation for the duration of the scan, which increases the chances of respiratory depression and airway obstructions. These feelings are frequently exhibited in children, which can lead to anxiety-related psychological disorders that continue into adulthood, such as claustrophobia. Studies suggest children experience similar levels of anxiety as adults.

In contrast, fNIRS is a non-invasive process that does not expose patients to confined spaces or magnetic fields. Compared to fMRI scans, fNIRS scans are less sensitive and can tolerate motion artifacts, which is important for patients with difficulty staying still. People with movement disorders would greatly benefit from this, as a larger threshold for assessment along with the lower temporal resolution allows for shorter scan times and increases patient comfort. One of the most important characteristics of fNIRS scans is their incredible portability and reduced cost compared to fMRI scans. This feature of the machine makes it very viable in clinical settings that allow for greater accessibility to brain imaging (Hallowell, Stewart, de Amorim e Silva, Ditchfield, 2007). One of the biggest strengths of fNIRS machines is its ability

to integrate with other neurocognitive devices, like electroencephalography (EEG). This pairing improves the brain-computer interface technologies including the spatial resolution from fNIRS and temporal resolution of EEG. This aids in mapping areas of brain activity, which can have potential treatment applications in psychological disorders such as anxiety.

Despite all the practical advantages of fNIRS, fMRI does offer certain improvements in data and quality. Primarily, fMRI is fMRI capable of whole brain metrics which allows researchers to observe hemodynamics in all regions of the brain. While advantageous in certain aspects, whole brain scans can be excessive for studies that are looking to only observe a select few regions of the brain. Furthermore, scans provide high spatial resolution, so researchers can precisely pinpoint brain activity within specific regions of interest (Bandettini et al., 1992). This advantage is critical for mapping functional brain organization and identifying regions associated with particular cognitive functions or disorders. Moreover, detailed spatial information enables researchers to create precise brain functional connectivity maps, enhancing our understanding of the brain's functional architecture. Because fNIRS and fMRI share a common hemodynamic origin, it would be reasonable to hypothesize that fNIRS could be used to provide information on whole-brain connectivity by proxy (Plichta, 2006). In other words, fNIRS has the potential to reproduce, to an extent, the functional networks generated using fMRI. Recent studies have conferred the feasibility of this conjecture. In 2011, a study documented that functional connectivity maps derived from resting-state fNIRS data were reproducible at the group level. Moreover, later studies have shown that resting-state fNIRS data is also reproducible on an intra-subject level. This study aims to analyze cortical neural hemodynamics during resting-state using fNIRS for future collation with fMRI data and applications in whole brain RSFC research. Between these modalities, an established correlation could mean expanding the horizons of

neuroimaging research. The utilization of fNIRS could potentially mitigate the contraindications associated with fMRI, thereby enhancing accessibility and facilitating a deeper understanding of brain function across diverse populations and contexts.

2. Methodology

2.1. Participants

This prospective multimodal study was conducted in collaboration with the University of Massachusetts Chan Medical School to investigate the steady-state neural activity of healthy individuals and compare their data with patients experiencing chronic pain. The study involved seven participating healthy individuals over age 18, who underwent the multimodal neuroimaging utilizing fMRI and fNIRS imaging techniques. This report focuses on the fNIRS data analysis of the participants to better understand the cortical hemodynamics of the brain and the resulting data's prospective role and application in the complementary analysis of fMRI data.

The setup of a fNIRS machine involves several steps to ensure accurate and effective brain activity measurement. Sections 2.2 to 2.5 delineate a comprehensive overview of the experiment's setup and procedure.

2.2. Sensor and Optode Placement

The scan involves using a skull cap containing optodes, which are the light-emitting and light-detecting components of the procedure. The optodes are arranged on the scalp to monitor specific brain regions. The placement is often guided by a standard brain atlas or based on the requirements of the study. The cap or band should be snug but comfortable to maintain optimal sensor contact with the scalp without causing discomfort to the participant. As a result, there are different sizes for children over age two (42 to 48 centimeters) and adults (50 to 60 centimeters).

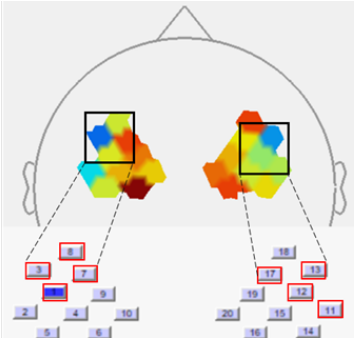

Figure 3: Optode placement map used in this study, a foundational component for the subsequent neural connectivity mapping

After samples are recorded, inferences can be made upon which brain regions were active, depending on the corresponding optode and area of the head for which that optode was placed. This study only utilizes 20 channels, therefore, only a select cortex region was analyzed. Figure 3 depicts the physical location of the optode placements, whereas Figure 4 shows the location key of the optodes utilized in this study.

Channel # (Left Hemisphere)	Channel # (Right Hemisphere)	Location	Location	Function
Ch 1	Ch 12	Precentral gyrus	lateral frontal lobe	voluntary motor movement
Ch 2	Ch 11	Postcentral gyrus	Lateral Parietal lobe	involuntary motor movement
Ch 3	Ch 13	Inferior frontal gyrus (Triangular)	frontal lobe (Broca's area)	processing of language (triangular - semantic processing of language)
Ch 4	Ch 15	Precentral gyrus	lateral frontal lobe	voluntary motor movement
Ch 5	Ch 14	Postcentral gyrus	Lateral Parietal lobe	involuntary motor movement
Ch 6	Ch 16	Central sulcus (Postcentral & Precentral gyri)	(central fissure) divides pre-& postcentral gyri along dorsal-ventral plane	motor and sensory function
Ch 7	Ch 17	Middle frontal gyrus	middle prefrontal cortex	Left (development of literacy), right (numeracy)
Ch 8	Ch 18	Middle frontal gyrus	middle prefrontal cortex	Left (development of literacy), right (numeracy)
Ch 9	Ch 19	Middle frontal gyrus	middle prefrontal cortex	Left (development of literacy), right (numeracy)
Ch 10	Ch 20	Superior frontal gyrus (Dorsolateral)	prefrontal cortex	higher cognitive functions/working memory

Figure 4: Functional description of optode channels

2.3. Calibration and Baseline Measurement

Before starting the measurement, the system is calibrated to ensure the accuracy of light detection and signal processing. A baseline measurement is often taken with the participant at rest or in a neutral state, to serve as a reference for detecting changes in brain activity.

2.4. Data Acquisition System Connection

Optodes are connected to the data acquisition system, which records the light signals. Before starting the experiment, it's crucial to check the quality of the signals to ensure that the optodes are functioning properly and are receiving clear signals.

2.5. Task Administration

Depending on the study design, participants may be asked to perform specific tasks or be exposed to certain stimuli while neural activity is recorded. Because this study focuses on collation methods with fMRI data, the recorded neural activity was sampled during resting-state. Resting-state fNIRS (also known as steady-state) measures the spontaneous hemodynamic fluctuations in the four lobes of the cerebral cortex of the brain (frontal, temporal, parietal, and occipital lobes) for patients who are not exposed to explicit tasks or stimuli [9].

2.6. fNIRS Software and use of NirsLab

After the experiment, collected data is analyzed using specialized software. This analysis includes filtering, signal correction, and statistical testing to interpret the brain activity patterns. fNIRS signals detect changes in light attenuation over several brain areas, including the somatosensory and motor regions, to measure the concentration changes in HbO and HbR in brain tissue. This data uses a series of time-dependent signals measured between each light source and the detector positions of the probes [xx]. The software used to record the data was done using NirsLab. This imaging system is intended for NIRS of blood perfusion movement in the brain region.

2.7. Data Pre-Processing

Channel signal visualization was completed in MATLAB using the files derived from the raw fNIRS data. The unfiltered signal data was plotted using a tiled chart layout to compare the signal quality across the individual channels. The oxygenated, deoxygenated, and total hemoglobin levels were plotted for each data sample to evaluate the amount of good channels established for each sample. A threshold number of channels was determined based on the prevalence of higher-quality channels across all the given data samples. By establishing a threshold, data samples with fewer functioning channels can be eliminated from consideration in later data analysis. This prevents the data from being skewed by outlier variables in signal quality.

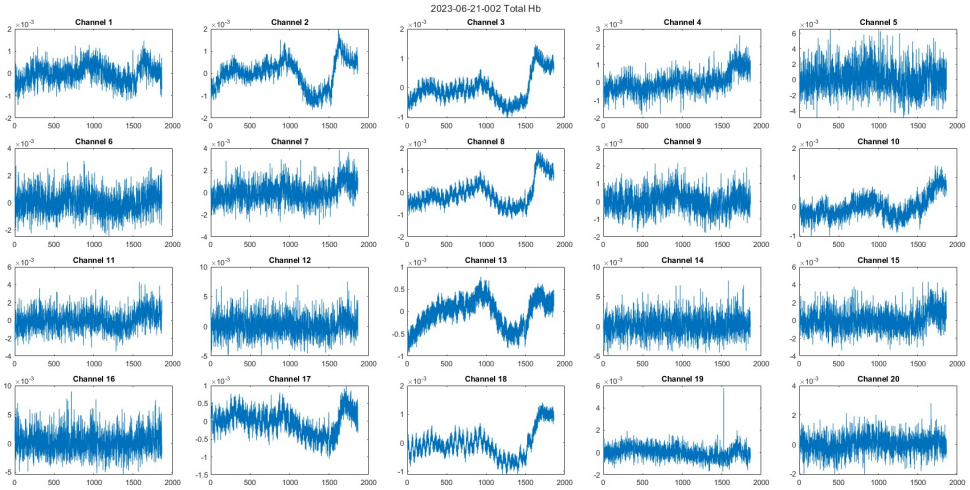

Figure 5: MATLAB generated graphs of the data recorded for each of the 20 channels for sample 2023-06-21_002 with complete data integrity

Analysis of the visualized channel data across all seven subjects revealed that every channel had varying levels of quality and consistency. Moreover, an assessment of channel quality across all subjects showed that 46.4% of channels were unreliable. In this context, no signal data was coming from those channels. The coefficient of variation (CV) for the instances

of unreliable channels across all subjects, as depicted in Figure 6, was adopted as the criterion to discern between channels exhibiting acceptable and subpar signal quality. This metric is automatically calculated using nirsLAB software and was computed at 15%. Specifically within this dataset, there are five channels with over four instances of poor signal quality across the samples. Furthermore, a subset of 12 channels (1, 3, 5, 6, 7, 9, 10, 11, 12, 13, 14, and 18) displayed a recurring pattern of having 3 instances of compromised or absent data.

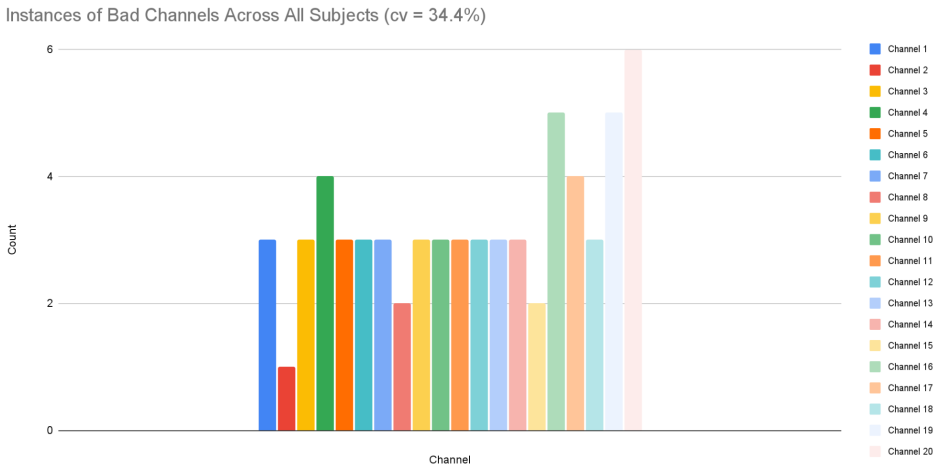

Figure 6: A graph of poor-quality channel instances across all the samples

A total of seven samples were collected for analytical purposes. To mitigate data dimensionality and ensure the integrity of subsequent analysis, subjects characterized by less than 50% of channels displaying good signal quality were discarded from the examined dataset. Here, Subjects 2023-06-21_001, 2023-07-07_002, and 2023-07-07_003 had 9, 7, and 2 good channels respectively, hence why these samples were removed from the analysis. By eliminating these samples, the remaining dataset's poor channel quality was reduced to 27.5%.

After establishing what samples would be considered in the final analysis, the raw data files were pre-processed and analyzed using nirsLAB. Data preprocessing was completed with SPM Level 1 using a generalized linear model (GLM) based analysis on each subject. GLM is a

statistical linear model utilized to arrange data by modeling it as a linear combination of an explanatory variable and an error term. In this context, a GLM measures the temporal variational pattern within the signals. This model is used as it represents fNIRS data better than other statistical models.

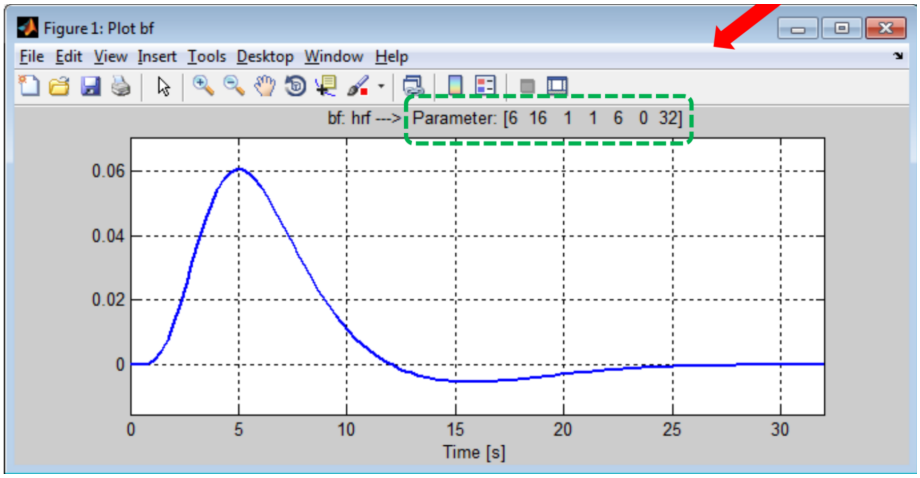

Figure 7: Baseline HRF curve used to model the expected pattern of changes in hemoglobin concentration over time in response to a task or stimuli

In nirsLAB, the data was truncated and checked for quality, but no filter was applied. The hemodynamic state parameters were from a Gratzer filter. The data was pre-whitened with AR(n) (NIRx's autoregression formula that is specifically suited towards fNIRS data) and a hemodynamic response function (HRF) was used as a basis function. There was no temporal filtering applied. The GLM coefficients were then estimated to create the SPM contrast data and a series of p and t values were saved as MATLAB files. These coefficients were stored visually as hemodynamic maps for the beta and residual mean square images, as shown in Figure 8. Additionally, statistical parameters and approximate beta values were calculated using MATLAB for each sample. The fNIRS data could be compared against the GLM to draw inferences about brain activity characteristics.

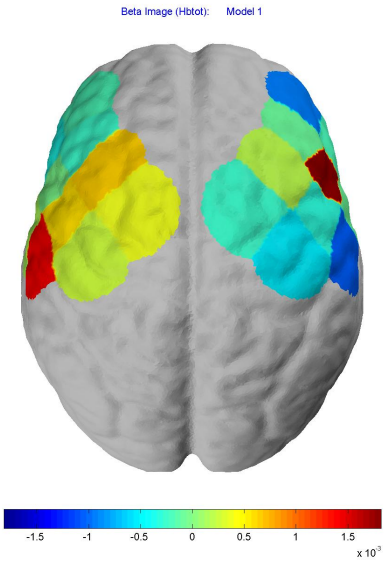

Figure 8: An example beta image hemodynamic map of the brain for sample 2023-06-21_002, where coloration denotes the magnitude of total hemoglobin measured during steady-state

After establishing the cortical neural hemodynamic maps, 2D resting-state functional connectivity matrices were generated to establish what nodes experienced signal synchrony. The matrices were created in MATLAB from the raw fNIRS data of each valid sample as shown in the figure below. Data was

normalized but was not standardized to prevent any skewing of the data. Nodes that were statistically significant were documented for later reference.

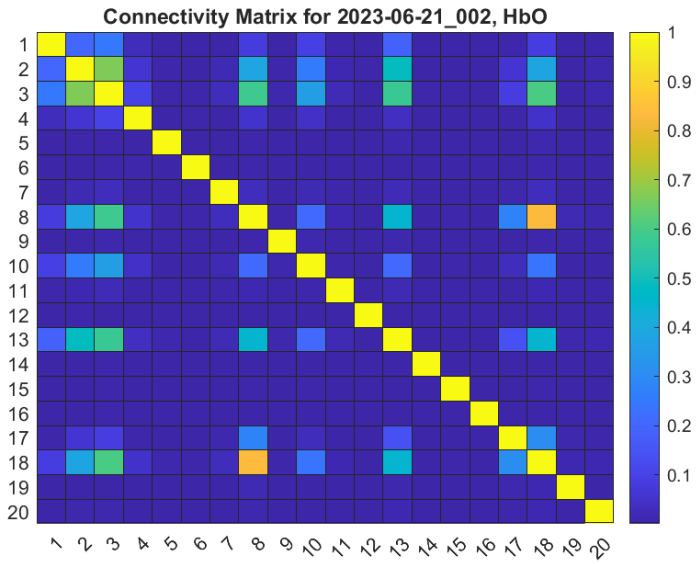

Figure 8.1: The connectivity matrix created for HbO levels for sample 2023-06-21_002

3. Results

Raw Data Across Channels (Sample 2023-06-21_002)

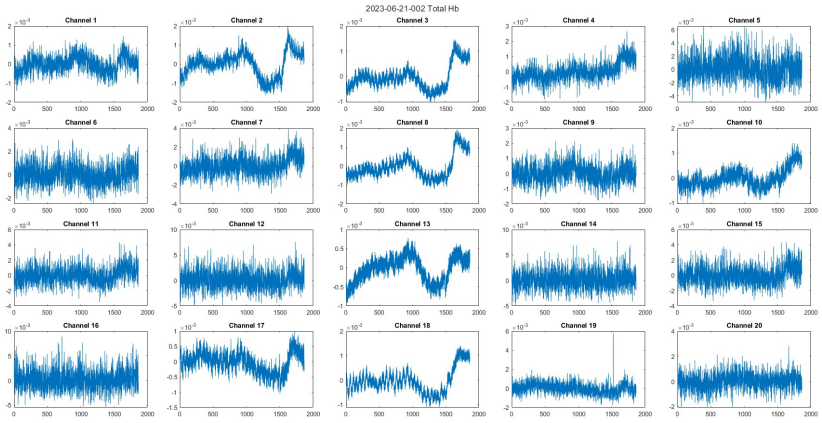

Figure 9: Raw data collection of sample 2023-06-21_002 for the total hemoglobin levels measured in each channel. Multiple channels indicate a sudden drop in HbR centralized around the front parietal lobe

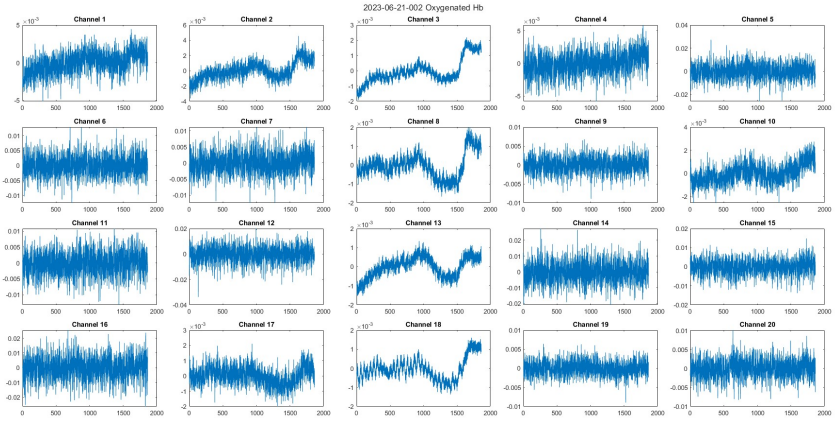

Figure 10: Raw data collection of sample 2023-06-21_002 for HbO levels measured in each channel

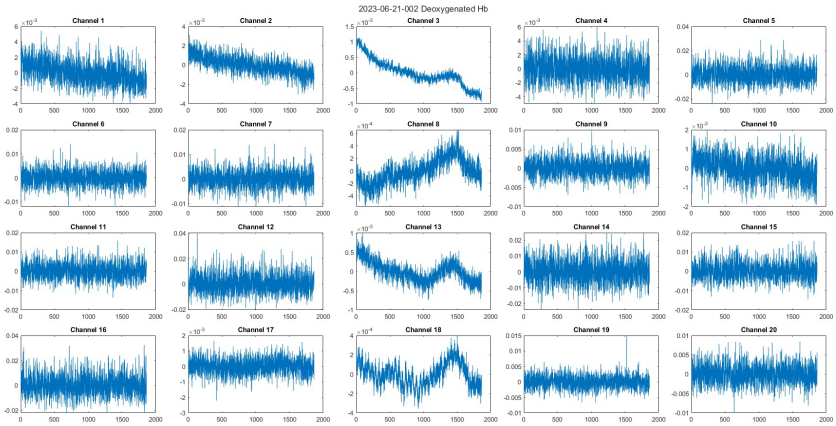

Figure 11: Raw data collection of sample 2023-06-21_002 for HbR levels measured in each channel

Neural Hemodynamic Maps (Sample 2023-06-21_002)

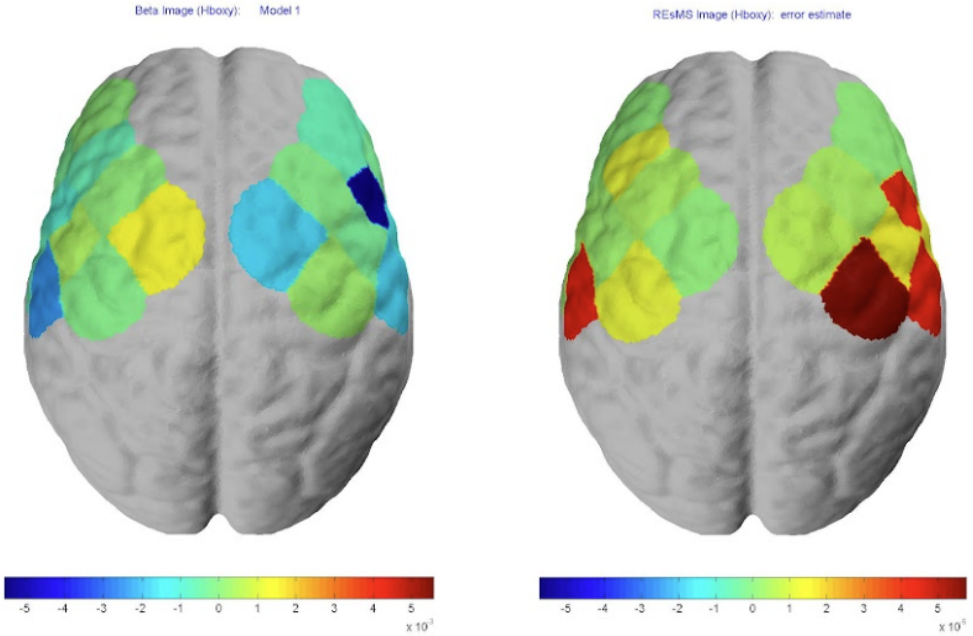

Figure 12: Left: The beta image hemodynamic map of the brain for sample 2023-06-21_002. Right: The residual mean square ('ResMS') image illustrating the residual values for the spatial distribution of the E matrix. The colors denote the magnitude of oxygenated hemoglobin measured during steady-state

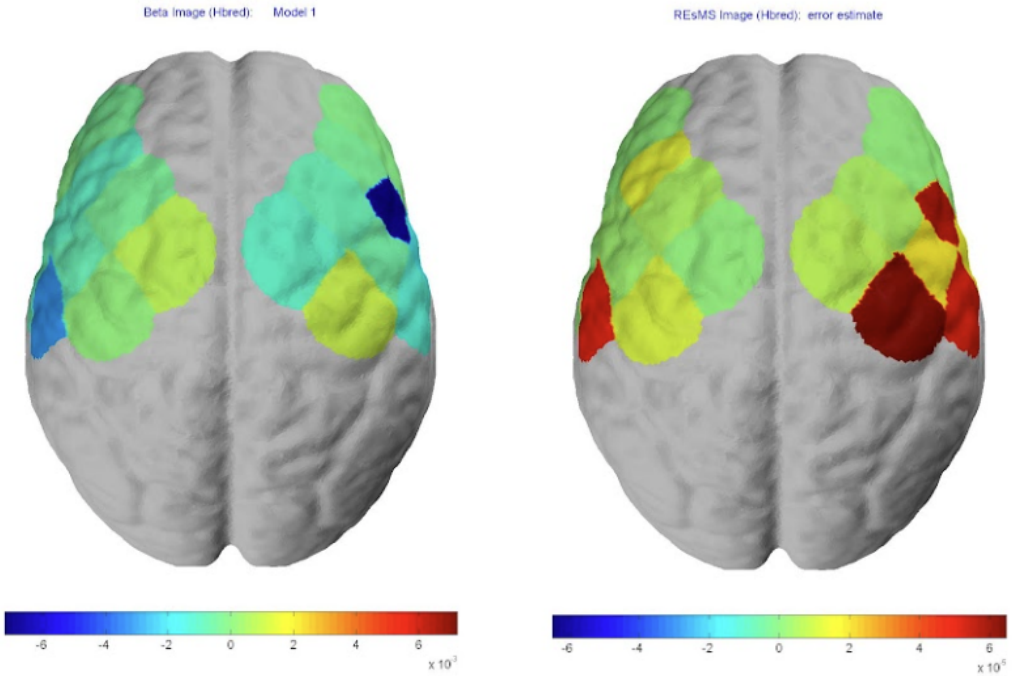

Figure 13: Left: The beta image hemodynamic map of the brain for sample 2023-06-21_002. Right: Illustration of the ResMS. The colors denote the magnitude of deoxygenated hemoglobin measured during steady-state

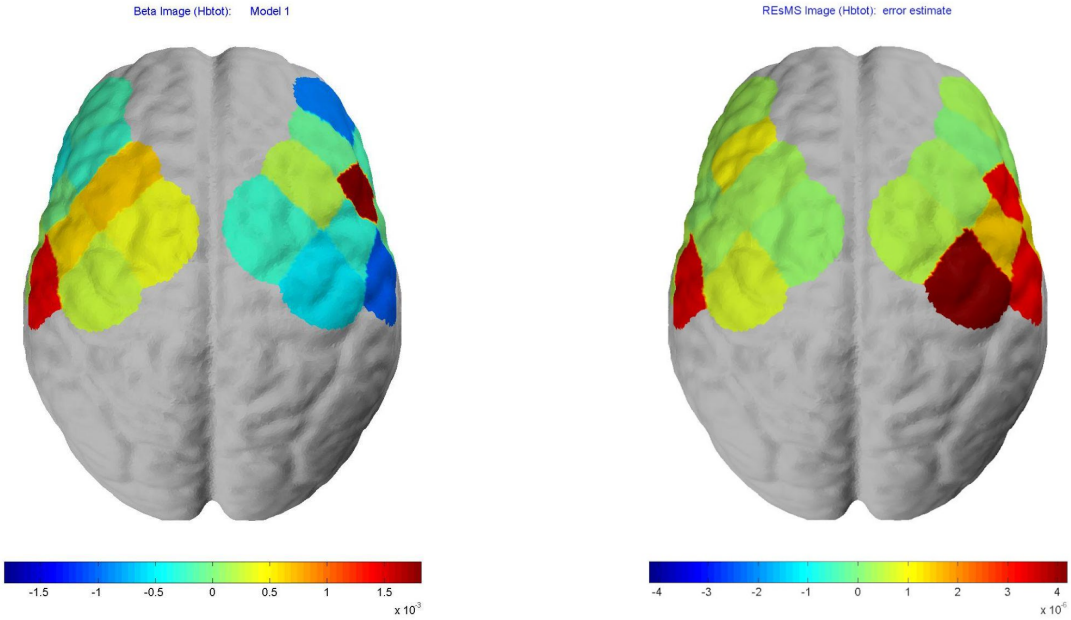

Figure 14: Left: The beta image hemodynamic map of the brain for sample 2023-06-21_002. Right: Illustration of the RedMS. The colors denote the magnitude of total hemoglobin measured during steady-state

Neural Hemodynamic Map Primary Activated Channels

Sample (OxyHb)	Primary Activated Channels (Beta Image)	Brain Region(s)	Cognitive Function
2023-06-21_001	2, 1	Postcentral gyrus, precentral gyrus	Voluntary motor movement, involuntary motor movement
2023-06-21_002	10	Superior frontal gyrus	Higher cognitive functions
2023-06-29_001	1, 6	Precentral gyrus, central sulcus	Voluntary motor movement, motor and sensory function
2023-06-29_002	2, 5	Postcentral gyrus, postcentral gyrus	Involuntary motor movement (both nodes)
2023-07-07_001	3, 8	Inferior frontal gyrus, middle frontal gyrus	Processing of language, development of literacy
2023-07-07_002	14	Postcentral gyrus	Involuntary motor movement
2023-07-07_003	N/A	N/A	N/A

Figure 15: Table of all the channels in which the oxygenated hemoglobin concentration was highest between samples

Resting-State 2D Connectivity Matrices (Sample 2023-06-21_002)

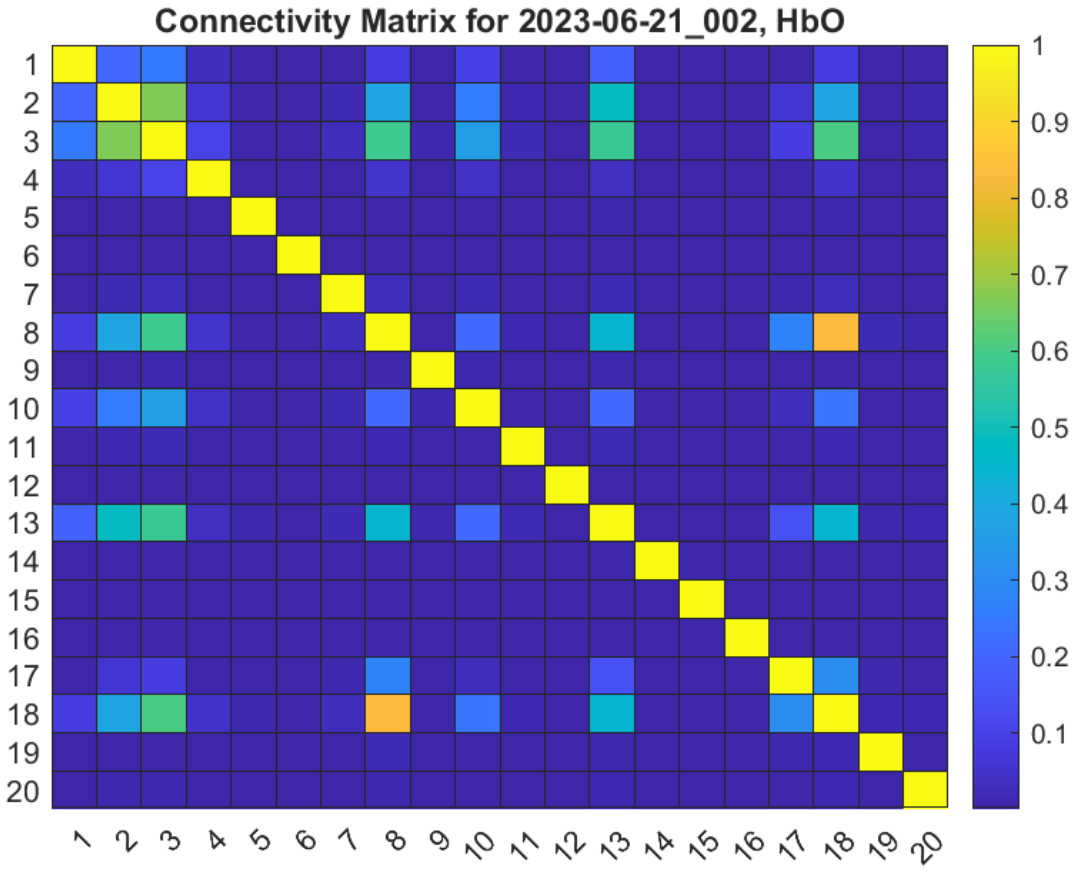

Figure 16: The connectivity matrix created for HbO levels for sample 2023-06-21_002

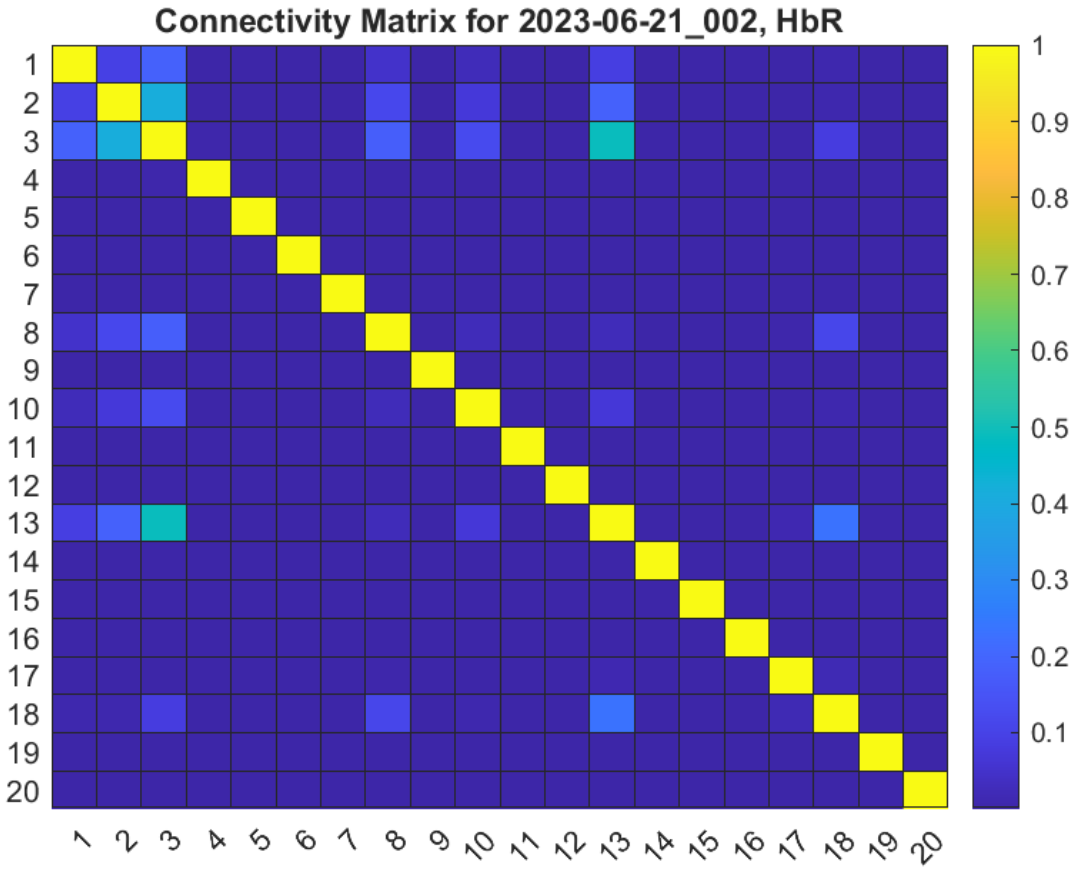

Figure 17: Connectivity matrix for HbR levels for sample 2023-06-21_002

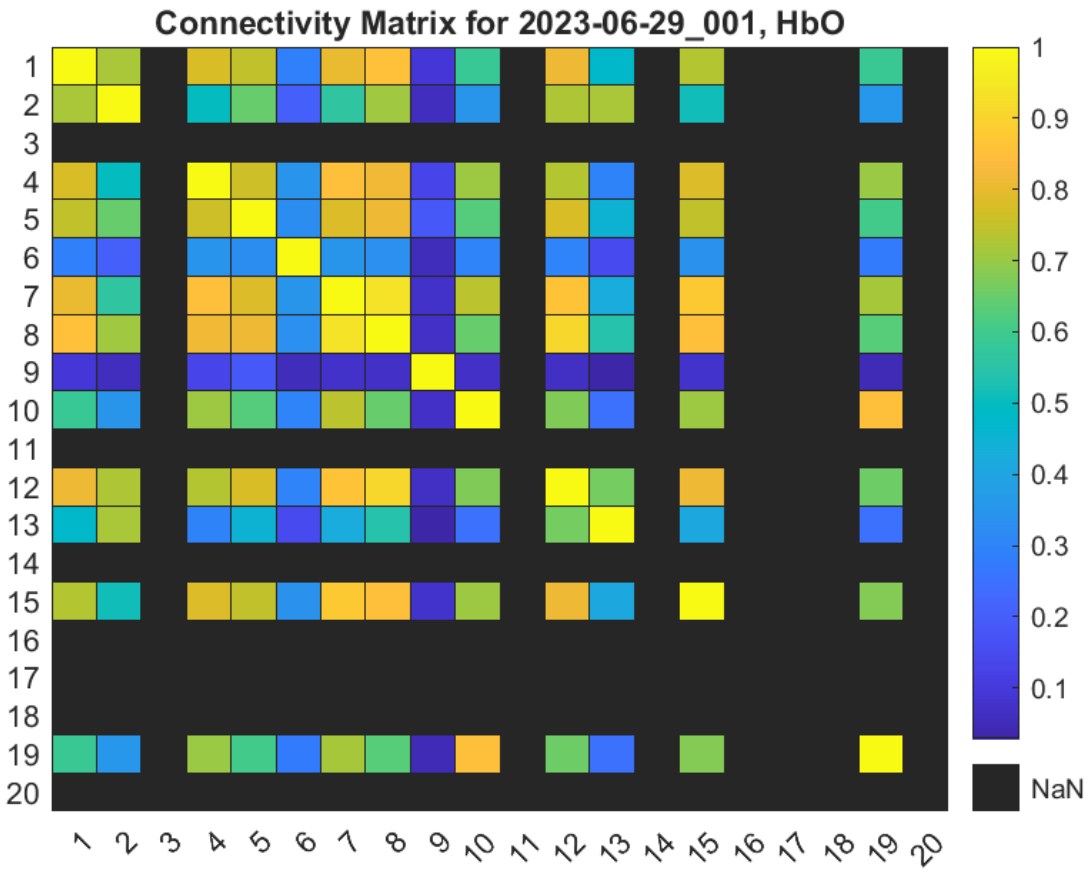

Figure 18: Connectivity matrix for HbO levels for sample 2023-06-29_001

2D Connectivity Matrices Channel Correlation Analysis (Sample 2023-06-21_002)

Correlated channels	Correlation Coefficient	Brain Region(s)	Cognitive Function
8 and 18	0.8351	Miggle frontal gyrus, middle prefrontal cortex	Literacy development, numeracy
2 and 3	0.6676	Postcentral gyrus, inferior frontal gyrus	Involuntary motor movement, processing of language
3 and 8	0.5823	Inferior frontal gyrus, middle frontal gyrus	Processing of language, literacy development
3 and 13	0.5753	Inferior frontal gyrus, frontal lobe (Broca's area)	Processing of language (both nodes)
2 and 13	0.4826	Postcentral gyrus, frontal lobe (Broca's area)	Involuntary motor movement, processing of language
8 and 13	0.4481	Middle frontal gyrus, inferior frontal gyrus	Literacy development, processing of language
13 and 18	0.4472	Frontal lobe (Broca's area), middle prefrontal cortex	Processing of language, numeracy
2 and 8	0.3855	Postcentral gyrus, middle frontal gyrus	Involuntary motor movement, literacy development
2 and 18	0.3808	Postcentral gyrus, middle prefrontal cortex	Involuntary motor movement, numeracy
3 and 10	0.3602	Inferior frontal gyrus, superior frontal gyrus	Processing of language, higher cognitive functions (working memory)

Figure 19: Connectivity Matrix values for HbO Sample 2023-06-21_002

4. Discussion

Looking at past literature, resting-state cortical neural hemodynamics are indicated by spontaneous increases or decreases in oxyhemoglobin. In the context of this study, which utilized GLM analysis to derive a mathematical model of the data in comparison to the expected baseline HRF curve as pictured in Figure 7, it was expected that there would be numerous potential outliers in the hemodynamic map data. The HRF curve assumes that an event/stimuli at a given time causes an increase in oxyhemoglobin levels. In resting-state neural analysis, increases in oxyhemoglobin would occur sporadically, which likely conflicts with the event-based analysis method. While this is not ideal for the given neural state being studied, it would provide valuable knowledge regarding whether the sample data aligns with the expected behaviors.

Following data preprocessing, the finalized set included four samples for analysis: 2023-07-07_001, 2023-06-29_002, 2023-06-29_001, and 2023-06-21_002. The average channel failure rate was 46.4%. The test administrator has noted that hair plays a role in the failure rate of channels. Hair may prevent a near-infrared emitter or a sensor channel from making appropriate contact with the scalp. Either case would cause affected sensor channels to have a reading of little to no magnitude, which are then detected as poor channels. After analyzing the data derived from the GLM analysis, a similar pattern of hemodynamics was found across the 4 valid samples as visualized in the beta images. For example, in sample 2023-06-21_002 as depicted in Figure 141, the left image, representing the beta image neural hemodynamic map for oxyhemoglobin, shows a relatively marginal increase in oxyhemoglobin in channel 10. Increased oxyhemoglobin in this channel corresponds to increased neural activity in the superior frontal gyrus which functionally, is responsible for higher cognitive function (working memory, executive control, planning linguistic communication…etc). Looking at Figure 18, which

displays the primary channel(s) that indicated increased neural activation as observed in the beta image, there was little to no similarity or overlap in primary channel activation across all of the samples observed. In other words, every sample had different cortical regions where increased oxyhemoglobin levels were measured. This would confer with the prior expectation that neural activity would be spontaneous, as it is unrelated to any event.

The neural hemodynamic maps for deoxyhemoglobin and total hemoglobin show a similar pattern of response. The distribution of responses again appears to be random (but proportionally related to the oxyhemoglobin neural hemodynamic maps), as expected since there was no coordinated task or stimuli to activate a specific brain region. Looking at Figure 12 which shows the deoxyhemoglobin neural hemodynamic map for sample 2023-06-21-002, we see a beta image that closely resembles the oxyhemoglobin map, where the level of deoxyhemoglobin is, however, notably lesser than that of oxyhemoglobin. This aligns with our prior expectations of neural activity and oxygen consumption. When a region of the brain is activated during either an event or spontaneously, the metabolic demand for oxygen and glucose increases, causing an increase in blood flow to the brain region(s) being activated. As oxyhemoglobin increases, deoxyhemoglobin decreases and the activated brain region experiences a net over oxygenation. A similar relationship between the oxyhemoglobin and deoxyhemoglobin neural hemodynamic maps was observed across the 4 valid samples.

An adjacency matrix, referred to as a connectivity matrix, is utilized to compare data-gathering node regions with areas of brain activity. For any connectivity matrix, the dimensions depend on the number of nodes in the system. In this particular case, there are 20 channels (nodes), yielding a matrix size of 20 by 20. Each data value of the connectivity matrix compares the similarity between two individual nodes. The more frequently these nodes exhibit signs of

coactivity, the greater the correlation between the two nodes. Connectivity matrices can be created for oxygenated, deoxygenated, and total hemoglobin levels. Oxygenated hemoglobin levels are the most indicative of brain activity, as shown in Figure 16. Deoxygenated hemoglobin levels can be useful as a secondary point of analysis, as shown in Figure 17, however, statistically significant levels of deoxygenated hemoglobin can represent anything from evidence of recent brain activity to no brain activity in the region.

Two factors to be considered in a connectivity matrix are weighting and directionality. Using weighting, the intensity of brain activity can be displayed such that the stronger node correlations have greater magnitudes than weaker ones. Directionality is a more complicated factor and is most useful for determining how one node affects other nodes. In a directed connectivity matrix, the behavior of one node directly influences one or more other nodes in a causal relationship. On the other hand, an undirected connectivity matrix does not provide this information but is useful for drawing simple activity correlations between nodes (Fornito, Bullmore, 2016). For this specific case, a weighted and undirected connectivity matrix was generated due to data collection constraints.

fNIRS scans are still novel and under development for brain activity applications, so the ultimate goal was to link the relationship between areas of activity in the brain, less so determining causal relationships. As shown in Figure 18 and the Appendix, the black regions represent poor data collection, where no conclusions can be drawn. For some of these scans, the data loss is low and relationships can be assessed with some scrutiny. For others, specifically the rejected samples with the largest number of non-functional channels, the data loss is significant and correlations cannot be corroborated. Each sample has three associated connectivity matrices; one for oxygenated hemoglobin (HbO), one for deoxygenated hemoglobin (HbR), and a

combined matrix of HbO and HbR levels. Full raw data collections and connectivity matrices are displayed in the Appendix for each sample.

Through analyzing sample 2023-06-21_002, several trends are apparent. The ten highest HbO level correlations for sample 2023-06-21_002 are displayed in Figure 19. The channels with the highest correlations are nodes 8 and 18, which correspond to literacy development and literacy. Another trend involves the generally significant correlations between nodes 2 and 3 and any other nodes, as node 2 corresponds to involuntary muscle movement while node 3 corresponds to language processing. It is encouraging to see that many of the strong correlations include regions of the brain associated with involuntary motor movements, especially for this steady-state analysis.

After data analysis, many of the samples yielded erroneous or inconclusive data because of the poor quality of the channels. It is visually apparent in the connectivity matrices of the sparseness of data, as illustrated in the connectivity matrices for HbO levels in Figure 24, Figure 48, Figure 54, and Figure 60 in the Appendix. For these samples, correlation coefficients are generally very low, staying around magnitudes of 0.1.

Figure 15 shows the channels for each respective (oxygenated) hemodynamic beta image map that showed the largest increase in oxygenated hemoglobin and its corresponding brain regions and functions for those optodes. Notably, there was little to no similarity observed between the samples which would confer with the notion of resting-state neural activity. An increase in brain region activity should be spontaneous because of a lack of events or stimuli. The regions that were most active between samples related to the voluntary and involuntary motor movement which could signify that participants either consciously or unconsciously moved during the scans.

5. Conclusion

Although fMRI and fNIRS can track hemodynamic changes in the brain, fMRI requires a heavy, expensive magnet while fNIRS requires a wearable, more affordable cap. The wider use of fNIRS would bring the ability to track hemodynamic neuroimaging to situations where an MRI is not practical or available. fNIRS is more accessible to subjects and clinicians with less time and money available and can greatly benefit studies involving more mobile tasks.

fNIRS must become more reliable to allow future studies and clinicians to track hemodynamic changes. In this case, 46.4% of the channels used in this study were unusable. Less than half of the channels were usable in three out of seven subjects. The causes of these unusable channels are not unique to this study. Insufficient contact between the scalp and near-infrared emitter or sensor channel yields erroneous data. The issue is compounded by the reality that this data loss disproportionately affects subjects with hair; the thicker the hair, the more the data collected on the subject is likely to be affected. This may make subjects less likely to be included in a viable dataset. Therefore, poor quality channels caused by hair may make initial data collection harder and affect the ability to use data from specific demographics. There are ethical concerns with excluding data from specific demographics from research, so future development must address this issue through designs or procedures.

Most importantly, these data results must be used alongside patient correspondence. These results can be used to analyze which regions are most active to aid in treatment options, but should not be used as evidence of a patient's conditions.

A significant compromise decided during data collection was using near-infrared lasers rather than LEDs. To collect fMRI data and fNIRS data simultaneously, the equipment for the fNRIS scans had to be safe for use in the MRI machine. This limited the use of LED optodes,

which cannot be used in strong magnetic fields. Using the LEDs would be more advantageous in creating a clearer dataset and may have reduced the number of poor channels observed in the analyzed dataset.

fNIRS holds significant promise within the neuroimaging realm as a valuable tool for measuring brain activity. Our hypothesis centers on fNIRS's potential to diagnose chronic pain by leveraging BOLD signals at the steady-state level. This is incredibly promising as the CDC estimates that 20.9 percent of adults in the United States experience chronic pain (Rikard, Strahan, Schmit, Guy Jr, 2023). However, enhancing the technique's design remains a critical focus area. This includes refining spatial resolution through advanced signal processing algorithms, integrating multimodal approaches, enabling real-time data analysis during neurocognitive training, and standardizing processes to ensure reproducibility across studies. These advancements are essential for elevating fNIRS into a more viable neuroimaging modality with practical applications in clinical settings.

6. References

1. Merskey, H. A. F. D. (1979). Pain terms: a list with definitions and notes on usage. Recommended by the IASP Subcommittee on Taxonomy. Pain, 6, 249-252.

2. Treede, R. D., Rief, W., Barke, A., Aziz, Q., Bennett, M. I., Benoliel, R., ... & Wang, S. J. (2015). A classification of chronic pain for ICD-11. Pain, 156(6), 1003-1007.

3. Verhaak, P. F., Kerssens, J. J., Dekker, J., Sorbi, M. J., & Bensing, J. M. (1998). Prevalence of chronic benign pain disorder among adults: a review of the literature. Pain, 77(3), 231-239.

4. Rikard, S. M., Strahan, A. E., Schmit, K. M., & Guy Jr, G. P. (2023). Chronic pain among adults—United States, 2019–2021. Morbidity and Mortality Weekly Report, 72(15), 379.

5. Robinson, M. E., Staud, R., & Price, D. D. (2013). Pain measurement and brain activity: will neuroimages replace pain ratings?. The Journal of Pain, 14(4), 323-327.

6. Davis, K. D., Flor, H., Greely, H. T., Iannetti, G. D., Mackey, S., Ploner, M., ... & Wager, T. D. (2017). Brain imaging tests for chronic pain: medical, legal and ethical issues and recommendations. Nature Reviews Neurology, 13(10), 624-638.

7. Scarapicchia, V., Brown, C., Mayo, C., & Gawryluk, J. R. (2017). Functional Magnetic Resonance Imaging and Functional Near-Infrared Spectroscopy: Insights from Combined

Recording Studies. Frontiers in human neuroscience, 11, 419. https://doi.org/10.3389/fnhum.2017.00419

9. Hu, Z., Liu, G., Dong, Q., & Niu, H. (2020). Applications of Resting-State fNIRS in the Developing Brain: A Review From the Connectome Perspective. Frontiers in Neuroscience, 14. https://doi.org/10.3389/fnins.2020.00476

9. Fornito, A., Zalesky, A., Bullmore, E. T., eds. Connectivity Matrices and Brain Graphs. *Fundamentals of Brain Network Analysis*. Published online 2016:89-113. doi:10.1016/b978-0-12-407908-3.00003-0

10. Abdalmalak, A., Novi, S. L., Kazazian, K., Norton, L., Benaglia, T., Slessarev, M., Debicki, D. B., Lawrence, K. St., Mesquita, R. C., & Owen, A. M. (2022). Effects of systemic physiology on mapping resting-state networks using functional near-infrared spectroscopy. *Frontiers in Neuroscience*, *16*. https://doi.org/10.3389/fnins.2022.803297

11. Benitez-Andonegui, A., Lührs, M., Nagels-Coune, L., Ivanov, D., Goebel, R., & Sorger, B. (2021). Guiding functional near-infrared spectroscopy optode-layout design using individual (f)MRI data: Effects on signal strength. *Neurophotonics*, *8*(02). https://doi.org/10.1117/1.nph.8.2.025012

12. Caulier-Cisterna, R., Appelgren-Gonzáles, J.-P., Oyarzún, J.-E., Valenzuela, F., Sitaram, R., Eblen-Zajjur, A., & Uribe, S. (2024). Comparison of LED- and laser-based fNIRS technologies to record the human peri-spinal cord neurovascular response. *Medical Engineering & Physics*, *127*, 104170. https://doi.org/10.1016/j.medengphy.2024.104170

13. Chong, J. S., Chan, Y. L., Ebenezer, E. G., Chen, H. Y., Kiguchi, M., Lu, C.-K., & Tang, T. B. (2020). FNIRS-based functional connectivity estimation using semi-metric analysis to study decision making by nursing students and registered nurses. *Scientific Reports*, *10*(1). https://doi.org/10.1038/s41598-020-79053-z

14. Hu, Z., Liu, G., Dong, Q., & Niu, H. (2020). Applications of resting-state fNIRS in the developing brain: A review from the connectome perspective. *Frontiers in Neuroscience*, *14*. https://doi.org/10.3389/fnins.2020.00476

15. Karim, H., Schmidt, B., Dart, D., Beluk, N., & Huppert, T. (2012). Functional near-infrared spectroscopy (FNIRS) of brain function during active balancing using a video game system. *Gait & Posture*, *35*(3), 367–372. https://doi.org/10.1016/j.gaitpost.2011.10.007

16. Lu, C.-M., Zhang, Y.-J., Biswal, B. B., Zang, Y.-F., Peng, D.-L., & Zhu, C.-Z. (2010). Use of fNIRS to assess resting state functional connectivity. *Journal of Neuroscience Methods*, *186*(2), 242–249. https://doi.org/10.1016/j.jneumeth.2009.11.010

17. Pinti, P., Tachtsidis, I., Hamilton, A., Hirsch, J., Aichelburg, C., Gilbert, S., & Burgess, P. W. (2018). The present and future use of functional near-infrared spectroscopy (FNIRS) for Cognitive Neuroscience. *Annals of the New York Academy of Sciences*, *1464*(1), 5–29. https://doi.org/10.1111/nyas.13948

18. Plichta, M. M., Herrmann, M. J., Baehne, C. G., Ehlis, A.-C., Richter, M. M., Pauli, P., & Fallgatter, A. J. (2006). Event-related functional near-infrared spectroscopy (FNIRS): Are the measurements reliable? *NeuroImage*, *31*(1), 116–124. https://doi.org/10.1016/j.neuroimage.2005.12.008

19. Scarapicchia, V., Brown, C., Mayo, C., & Gawryluk, J. R. (2017). Functional magnetic resonance imaging and functional near-infrared spectroscopy: Insights from combined recording studies. *Frontiers in Human Neuroscience*, *11*. https://doi.org/10.3389/fnhum.2017.00419

20. Hallowell, L. M., Stewart, S. E., de Amorim e Silva, C. T., Ditchfield, M. R. (2007). Reviewing the process of preparing children for MRI. Pediatric Radiology, 38(3), 271–279. https://doi.org/10.1007/s00247-007-0704-x

21. Fornito, A., Zalesky, A., Bullmore, E. T. Connectivity Matrices and Brain Graphs. (2016). In Fundamentals of Brain Network Analysis (pp. 89–113). Elsevier. https://doi.org/10.1016/b978-0-12-407908-3.00003-0

22. Rikard, S. M., Strahan, A. E., Schmit, K. M., & Guy Jr, G. P. (2023). Chronic pain among adults—United States, 2019–2021. Morbidity and Mortality Weekly Report, 72(15), 379.

7. Appendix

7.1. Sample 2023-06-21_001

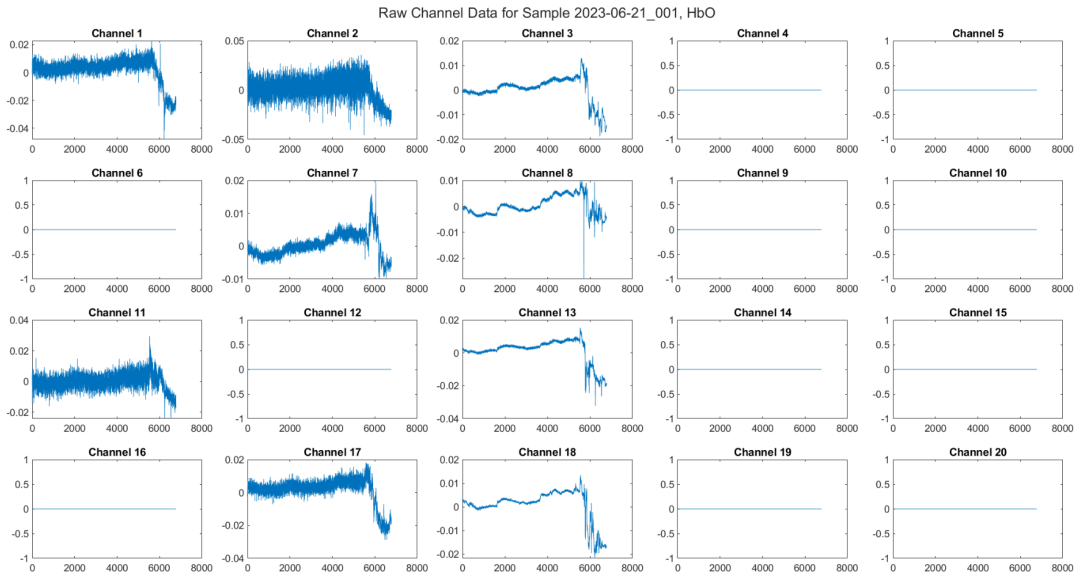

Figure 21: Raw data collection of sample 2023-06-21_001 for HbO levels measured in each channel

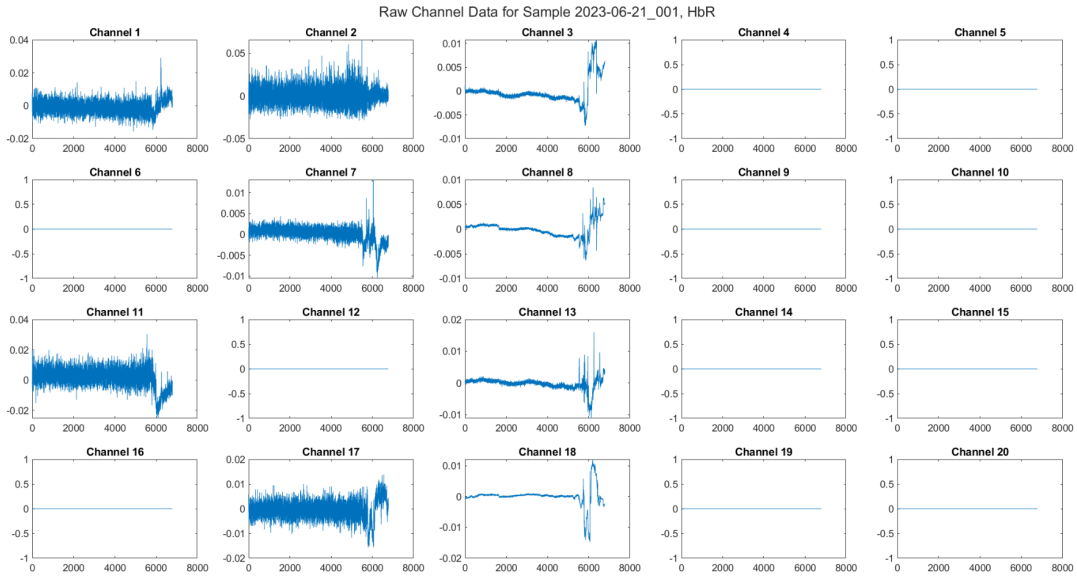

Figure 22: Raw data collection of sample 2023-06-21_001 for HbR levels measured in each channel

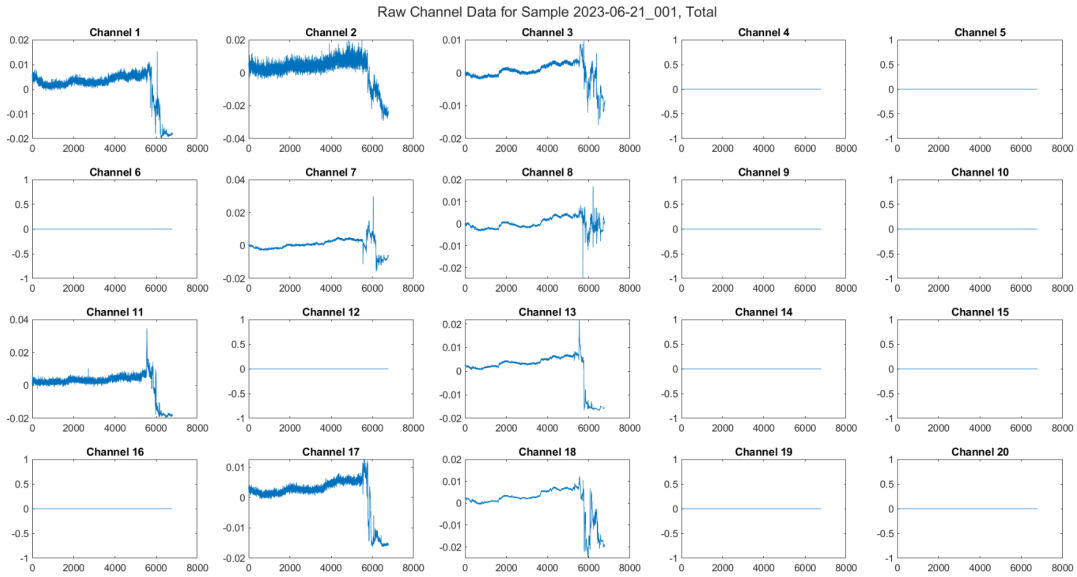

Figure 23: Raw data collection of sample 2023-06-21_001 for total hemoglobin levels measured in each channel

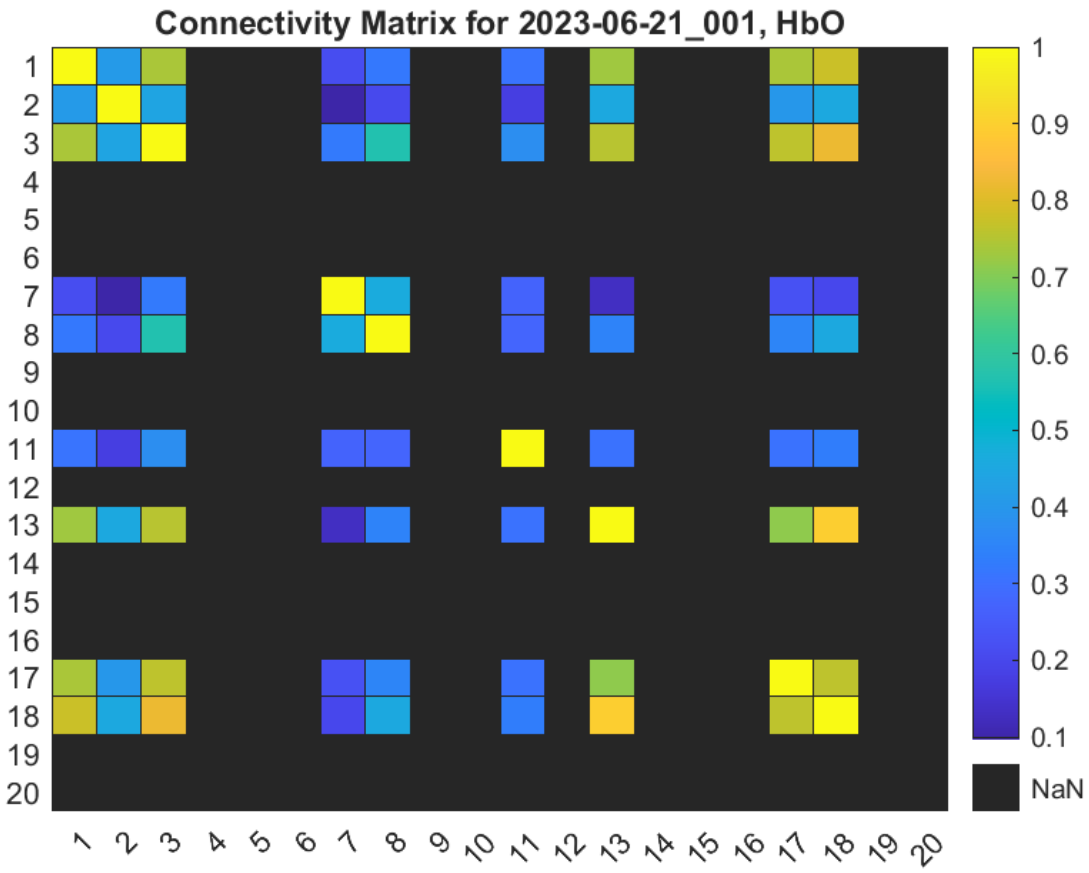

Figure 24: Connectivity matrix for HbO levels for sample 2023-06-21_001

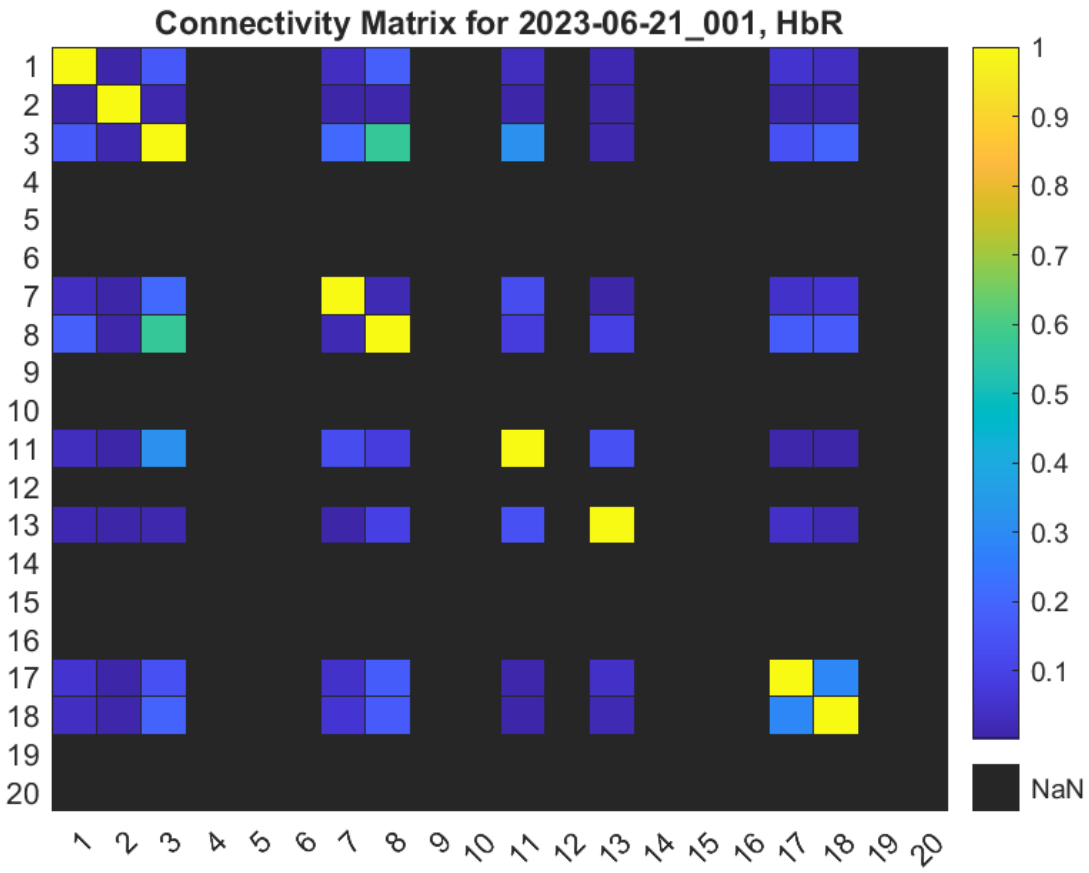

Figure 25: Connectivity matrix for HbR levels for sample 2023-06-21_001

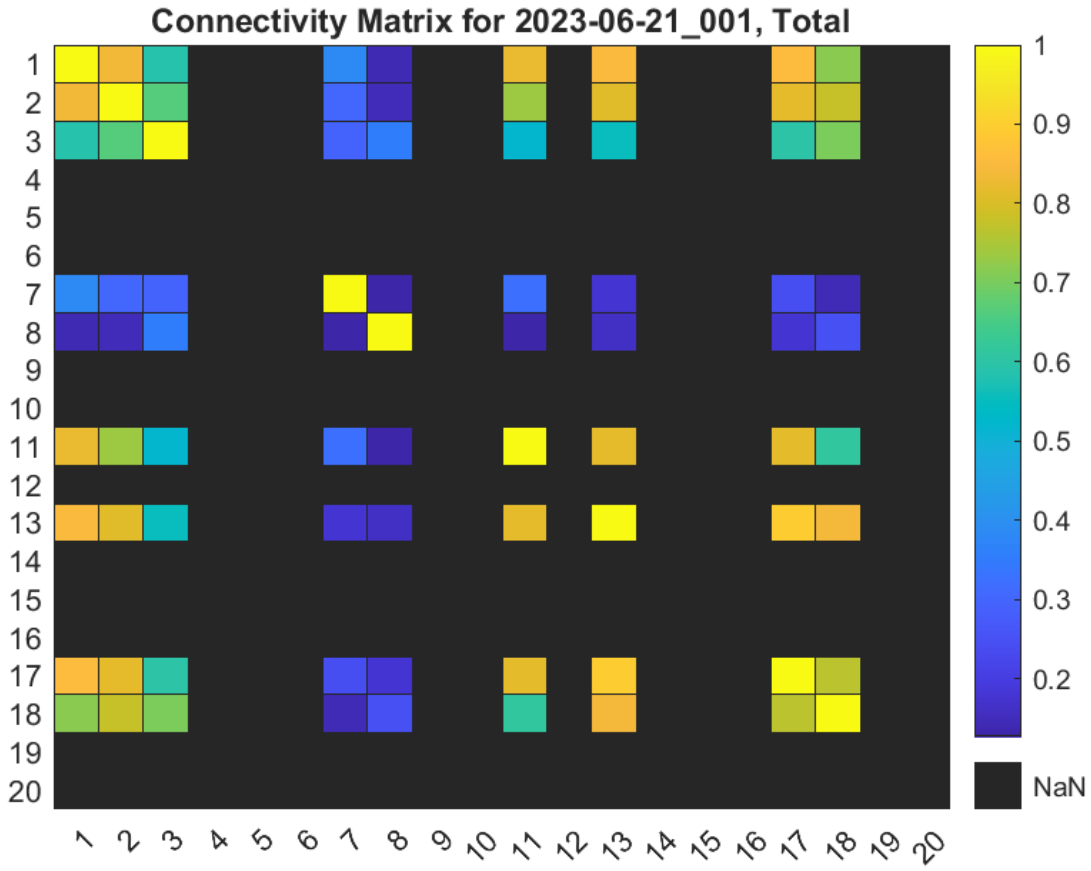

Figure 26: Connectivity matrix for total hemoglobin levels for sample 2023-06-21_001

7.2. Sample 2023-06-21_002

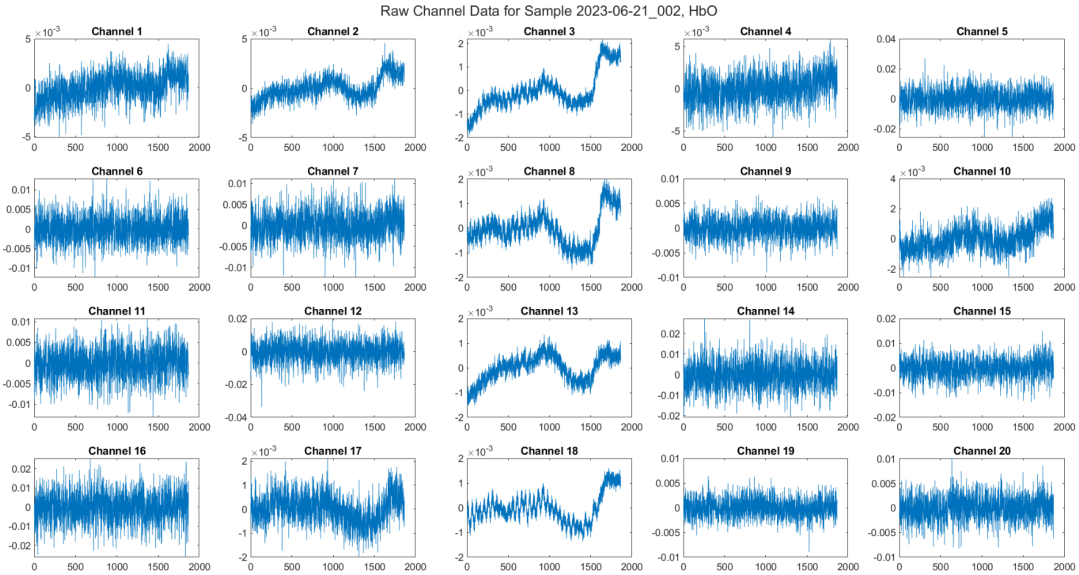

Figure 27: Raw data collection of sample 2023-06-21_002 for HbO levels measured in each channel

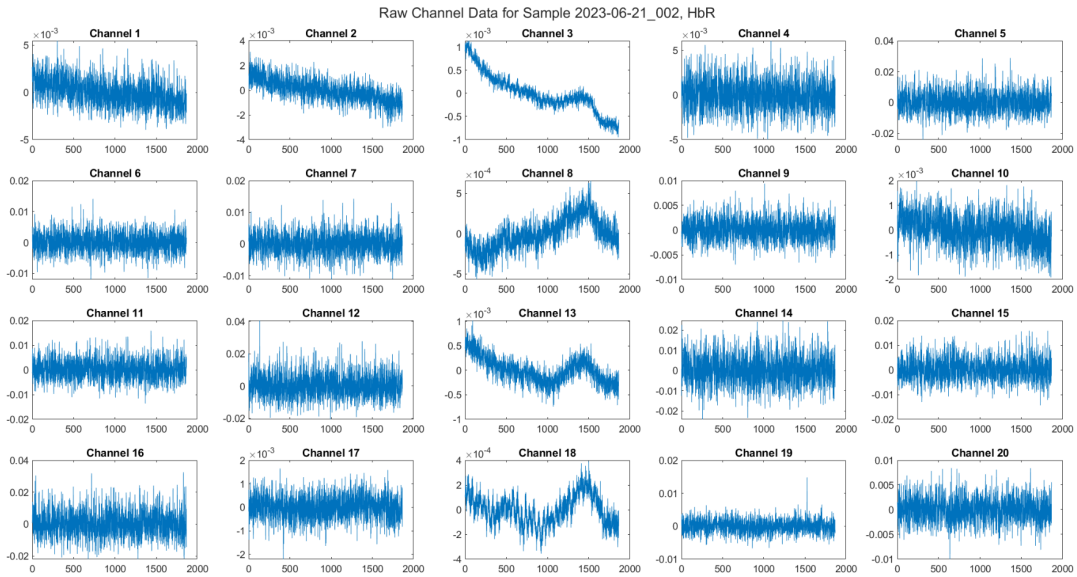

Figure 28: Raw data collection of sample 2023-06-21_002 for HbR levels measured in each channel

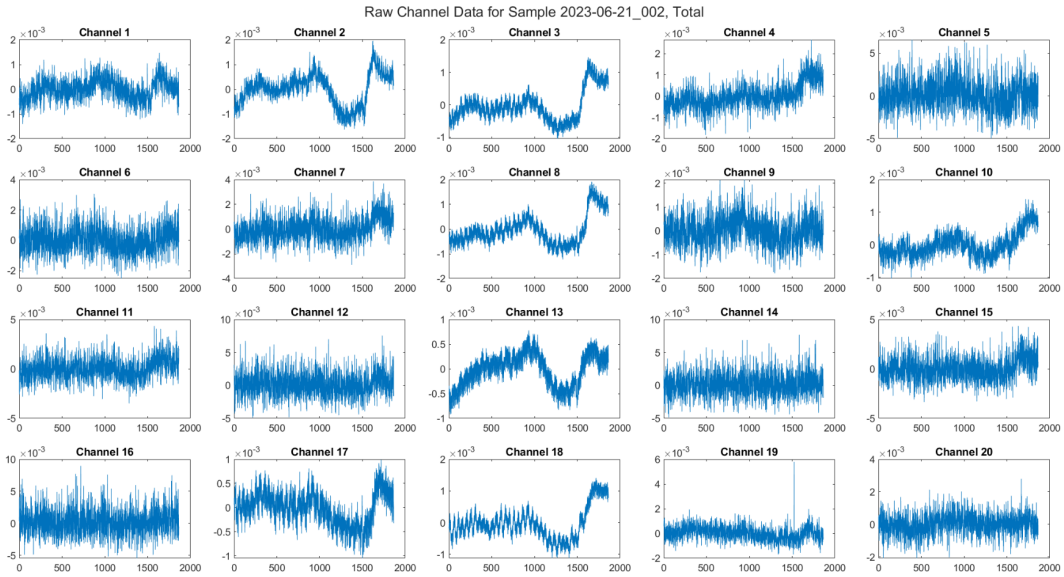

Figure 29: Raw data collection of sample 2023-06-21_002 for total hemoglobin levels measured in each channel

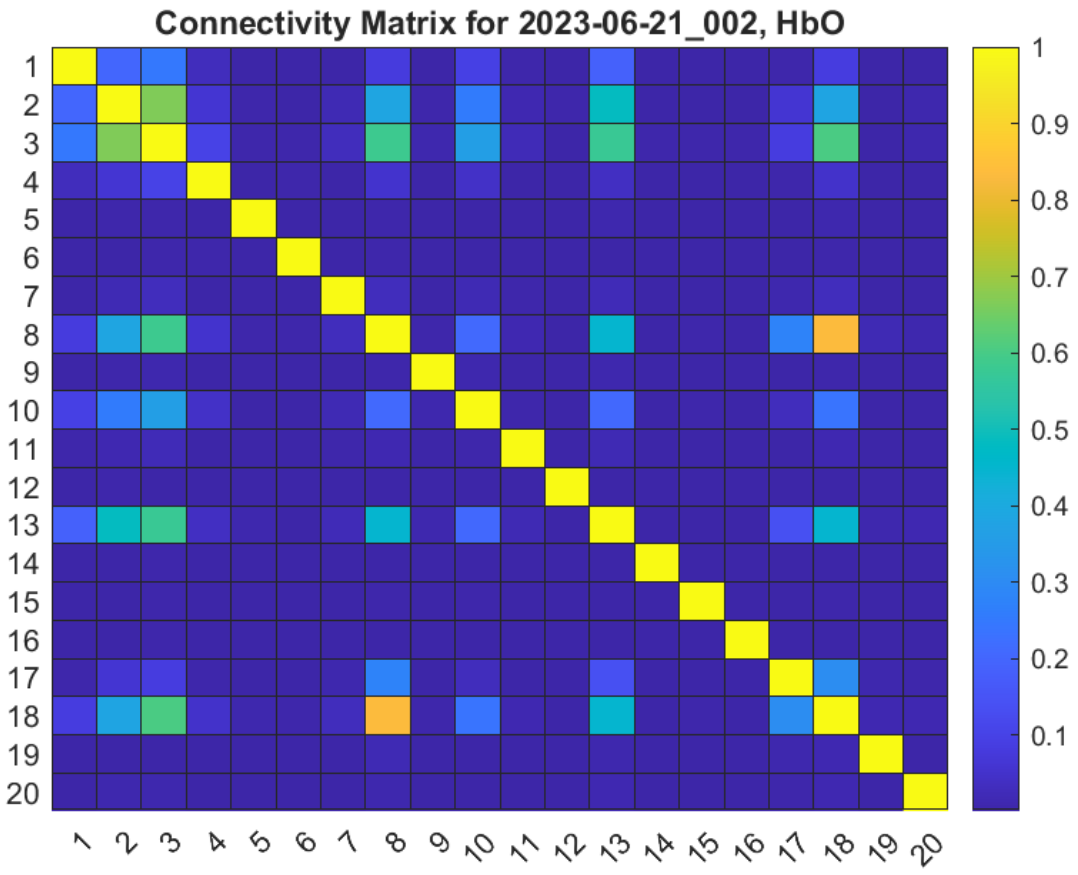

Figure 30: Connectivity matrix for HbO levels for sample 2023-06-21_002

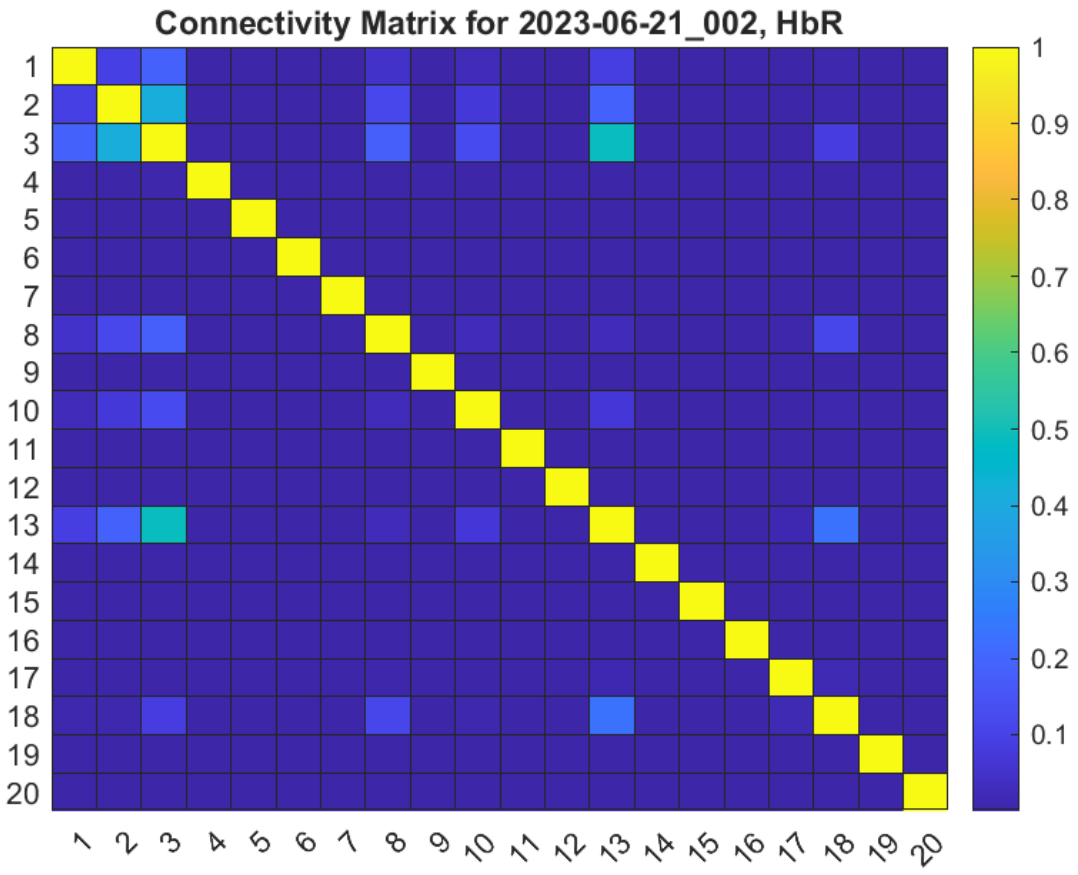

Figure 31: Connectivity matrix for HbR levels for sample 2023-06-21_002

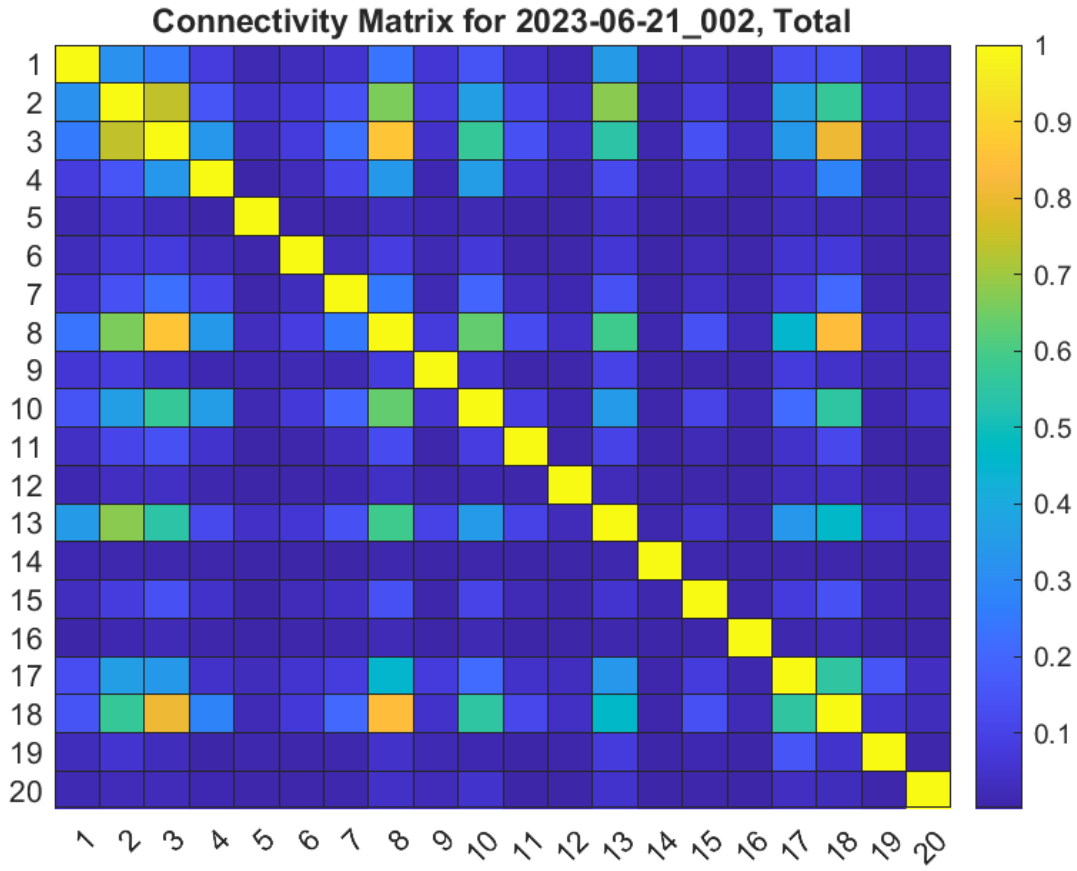

Figure 32: Connectivity matrix for total hemoglobin levels for sample 2023-06-21_002

7.3. Sample 2023-06-29_001 (NEEDS TOTAL)

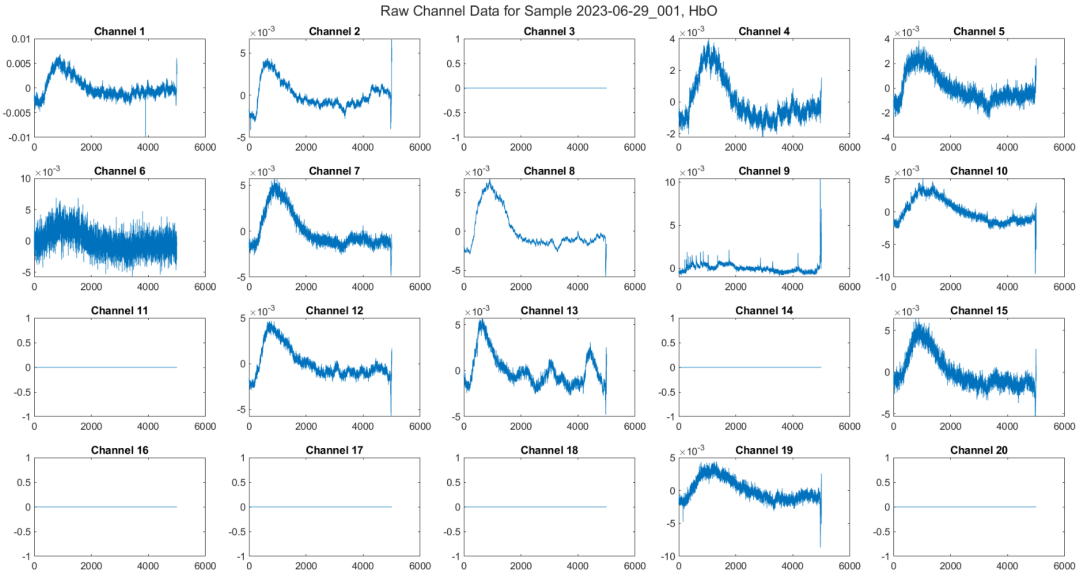

Figure 33: Raw data collection of sample 2023-06-29_001 for HbO levels measured in each channel

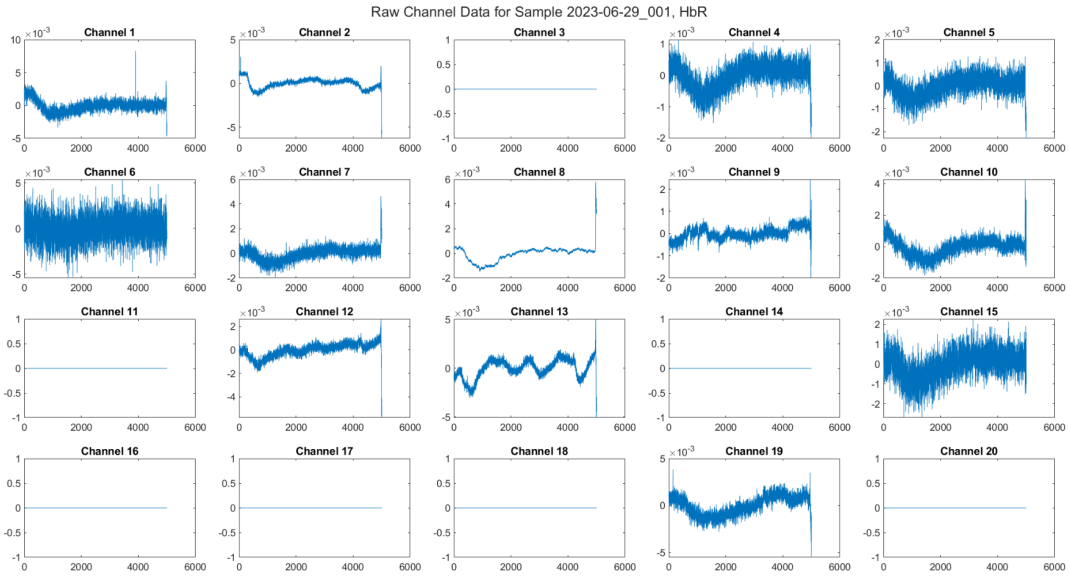

Figure 34: Raw data collection of sample 2023-06-29_001 for HbR levels measured in each channel

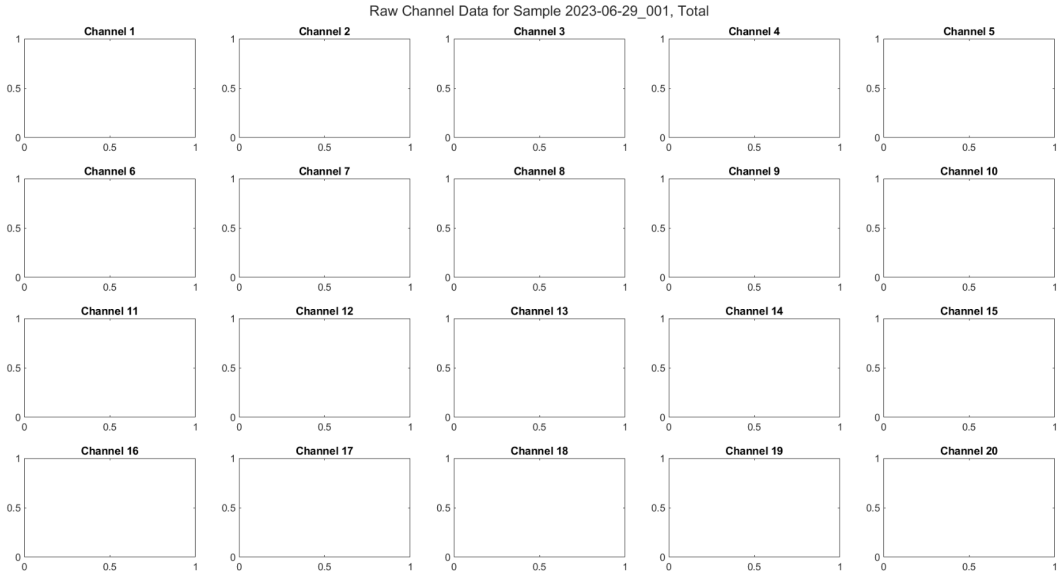

Figure 35: Raw data collection of sample 2023-06-29_001 for total hemoglobin levels measured in each channel

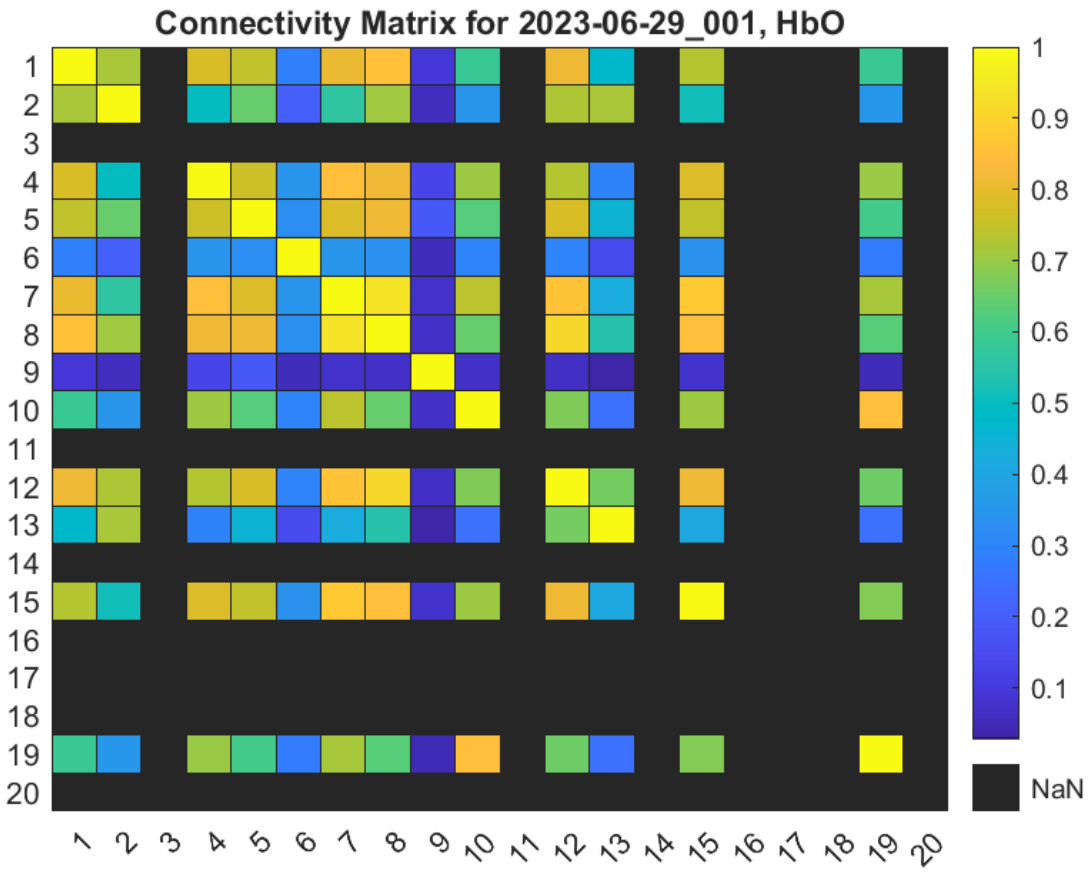

Figure 36: Connectivity matrix for HbO levels for sample 2023-06-29_001

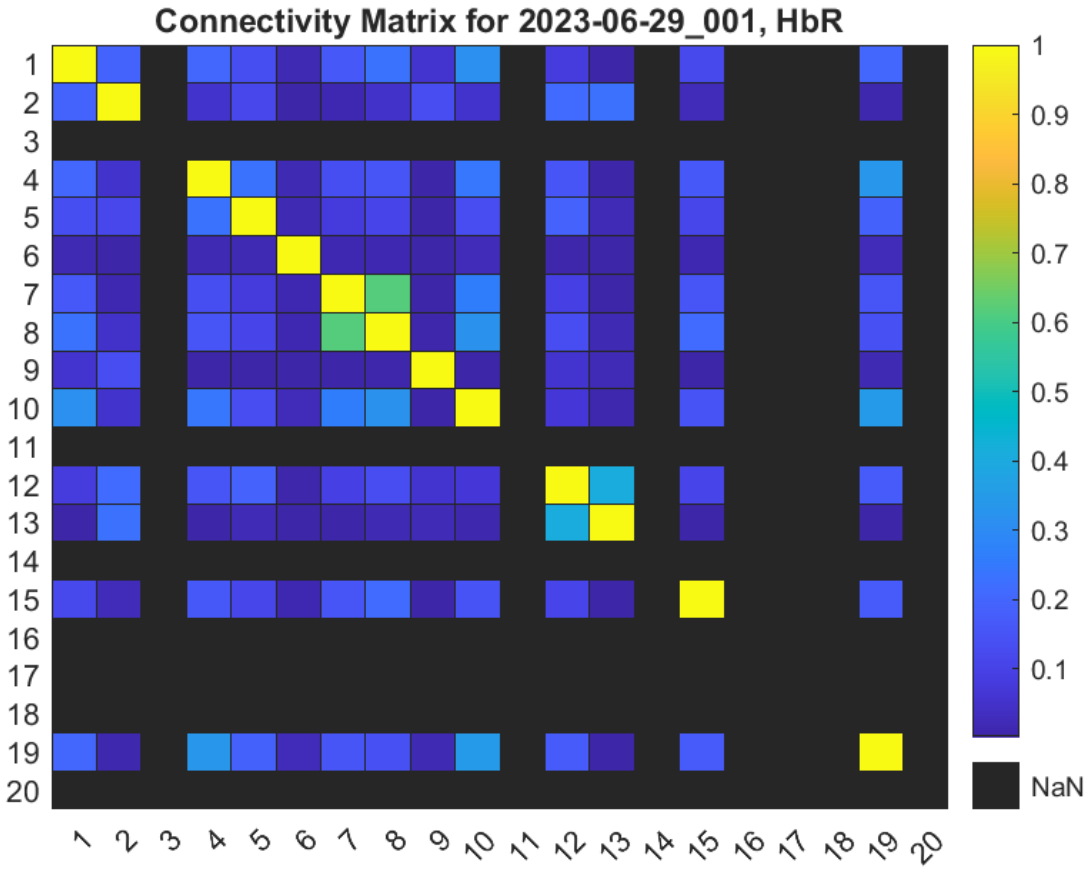

Figure 37: Connectivity matrix for HbR levels for sample 2023-06-29_001

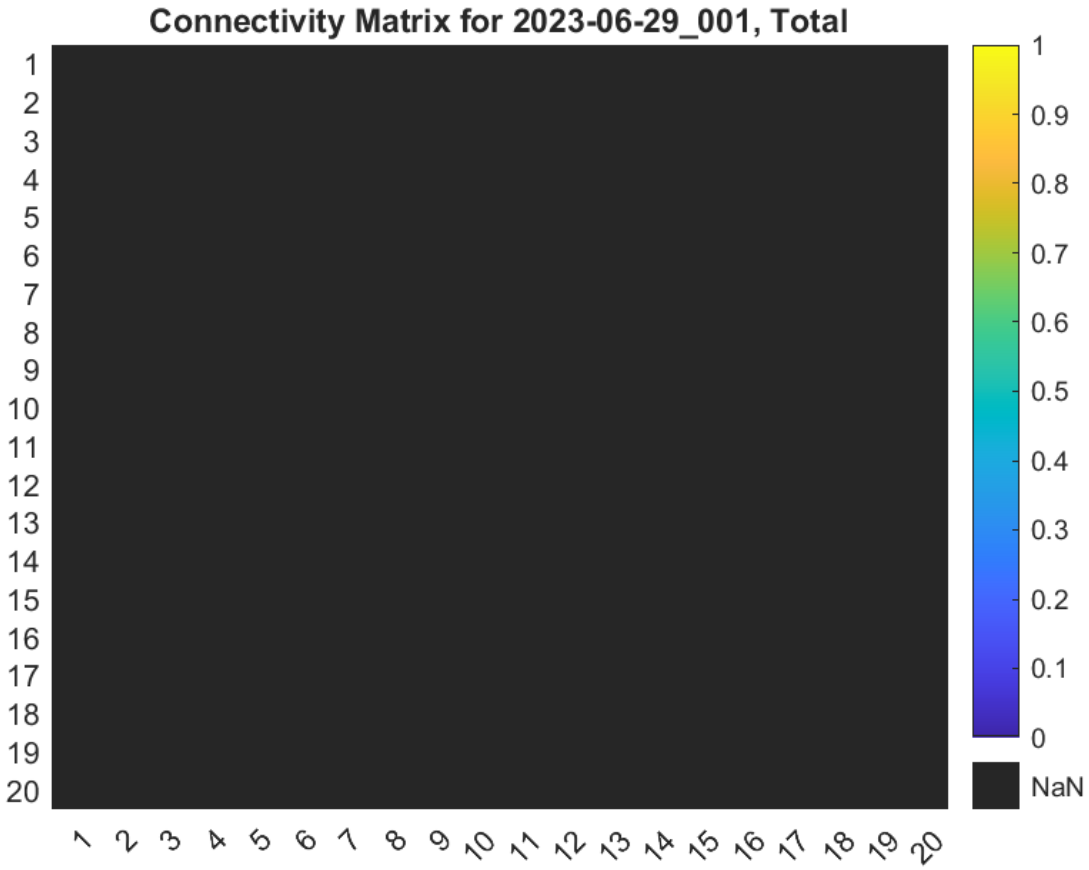

Figure 38: Connectivity matrix for total hemoglobin levels for sample 2023-06-29_001

7.4. Sample 2023-06-29_002

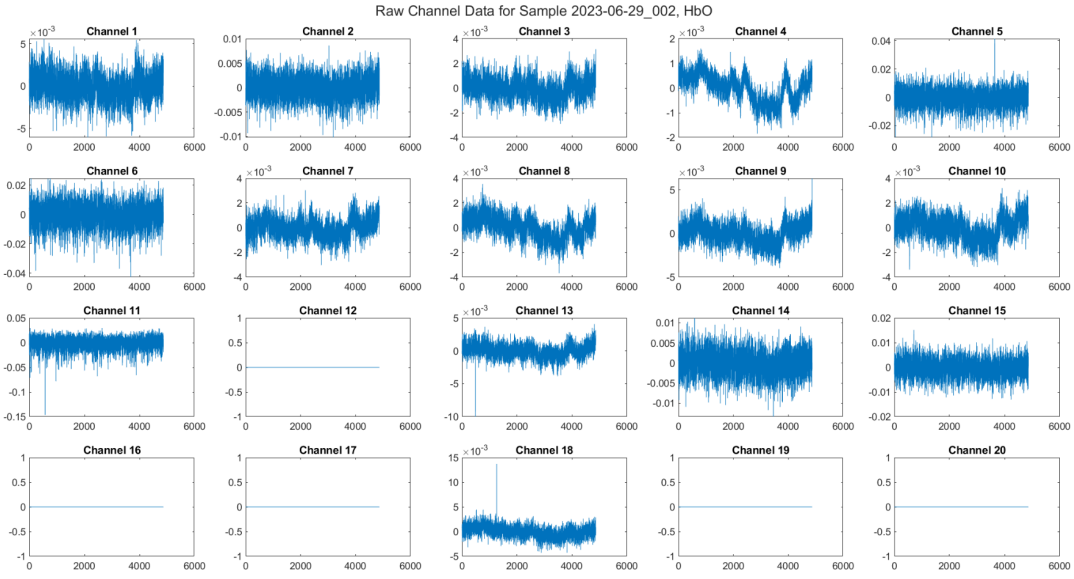

Figure 39: Raw data collection of sample 2023-06-29_002 for HbO levels measured in each channel

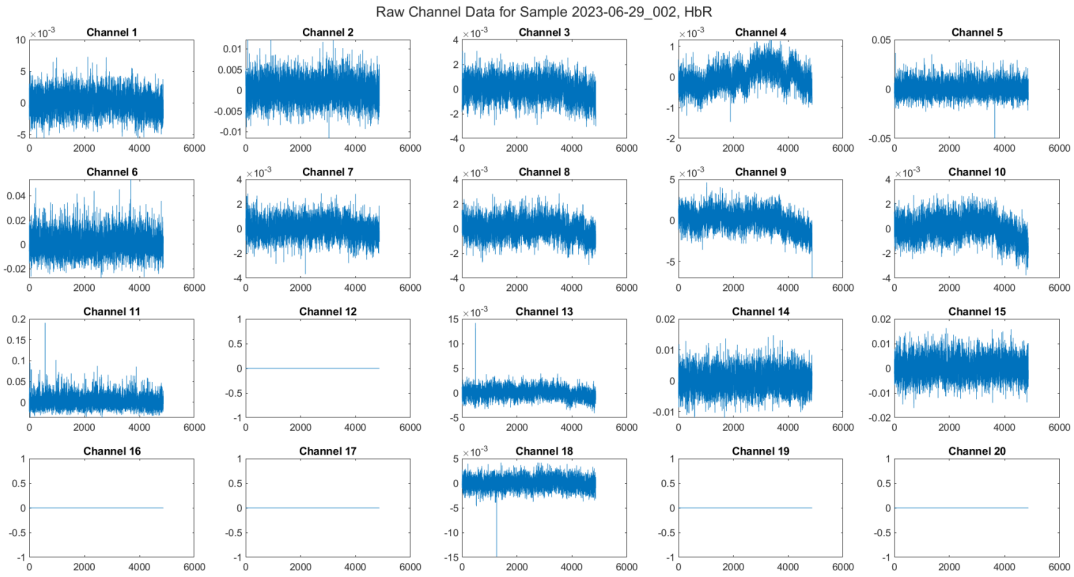

Figure 40: Raw data collection of sample 2023-06-29_002 for HbR levels measured in each channel

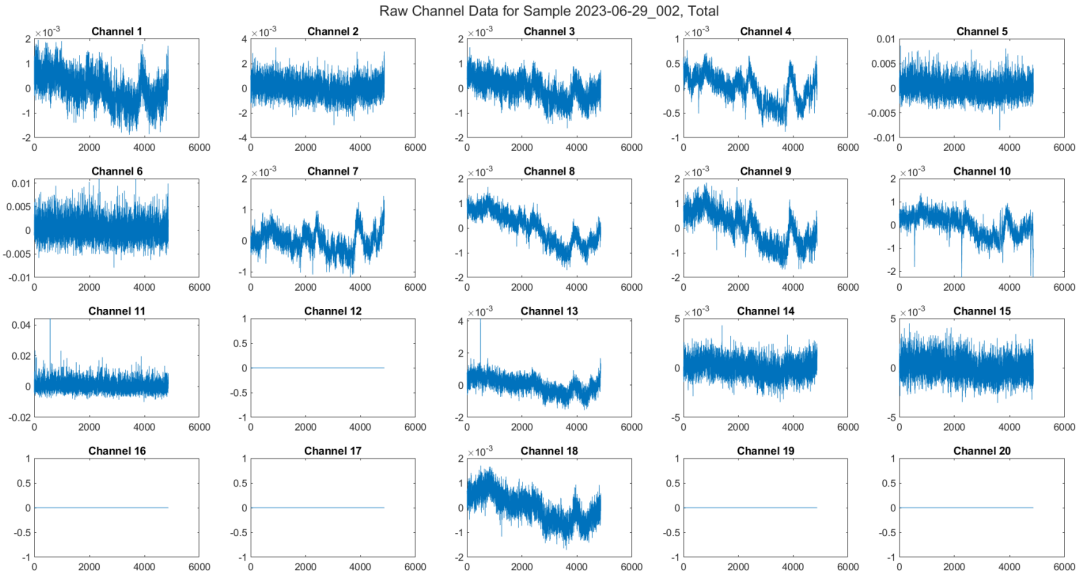

Figure 41: Raw data collection of sample 2023-06-29_002 for the total hemoglobin levels measured in each channel

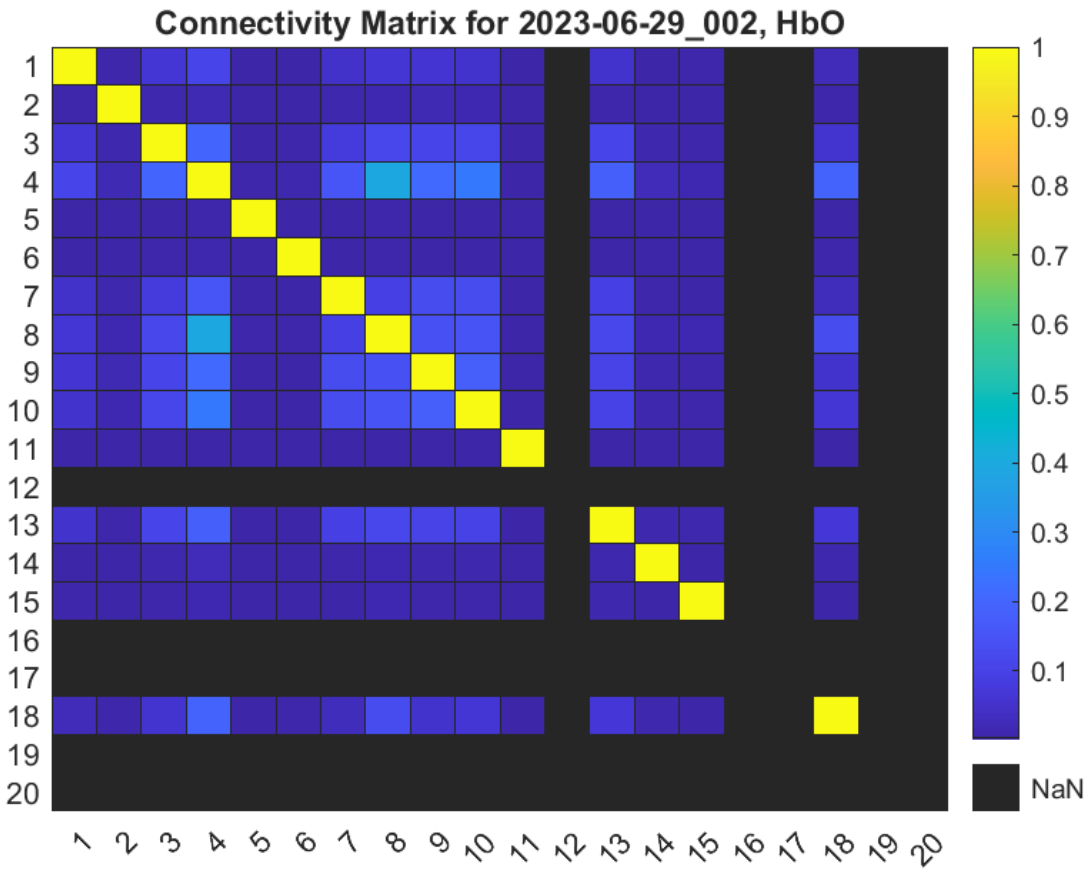

Figure 42: Connectivity matrix for HbO levels for sample 2023-06-29_002

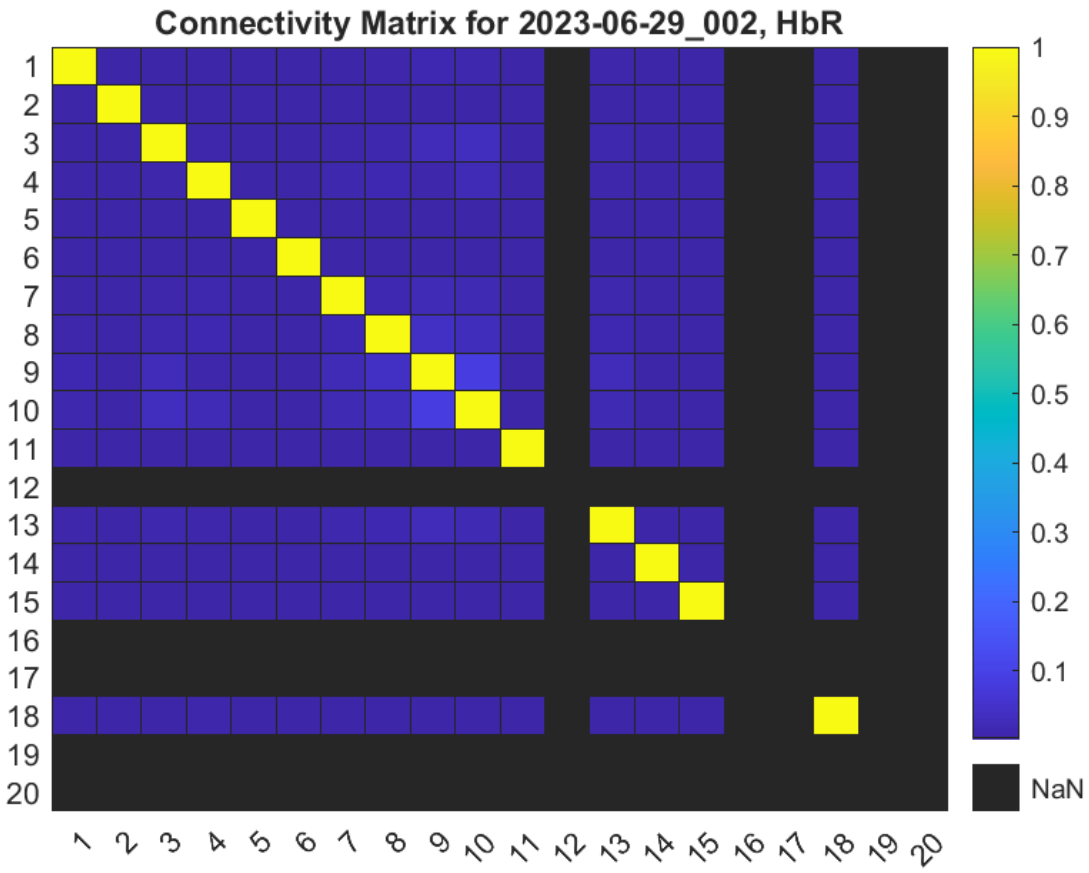

Figure 43: Connectivity matrix for HbR levels for sample 2023-06-29_002

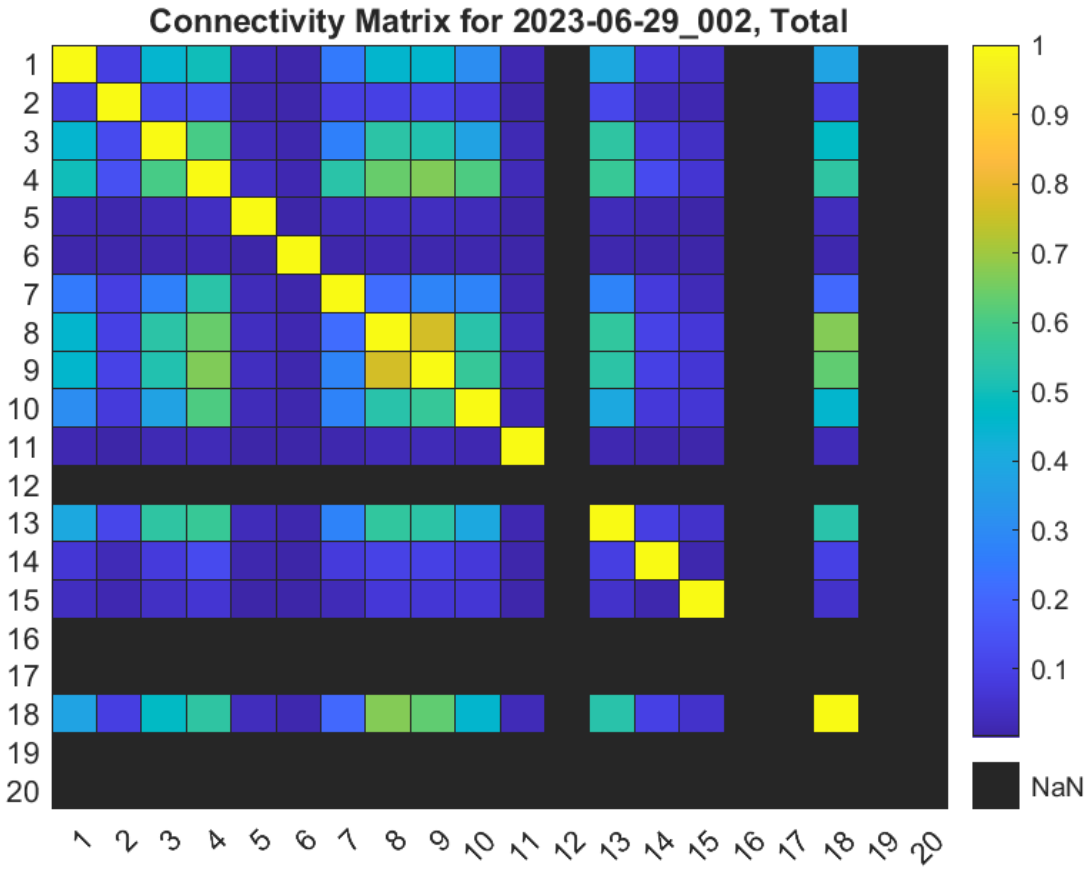

Figure 44: Connectivity matrix for total hemoglobin levels for sample 2023-06-29_002

7.5. Sample 2023-07-07_001

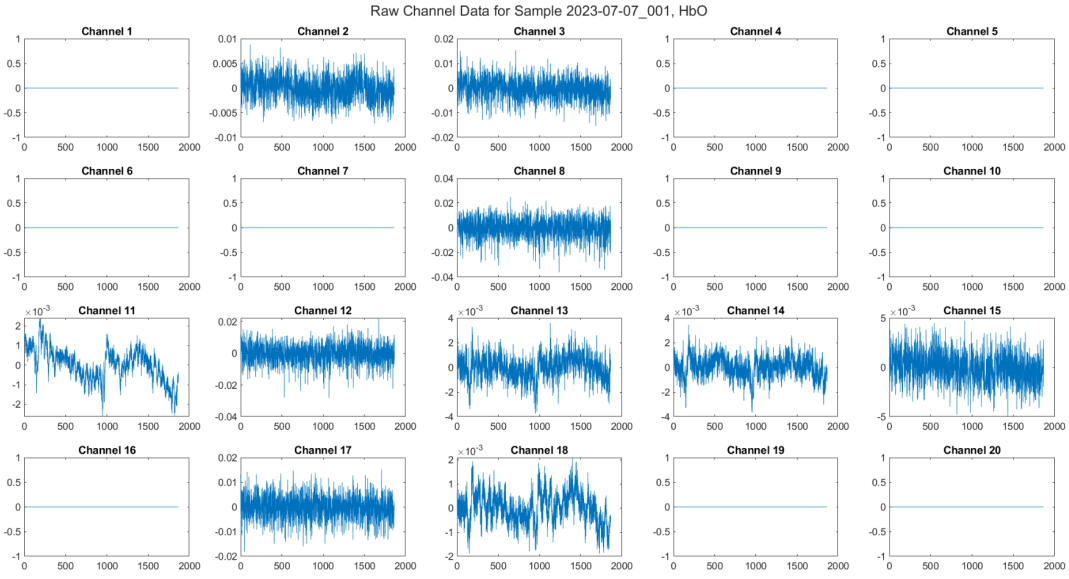

Figure 45: Raw data collection of sample 2023-07-07_001 for HbO levels measured in each channel

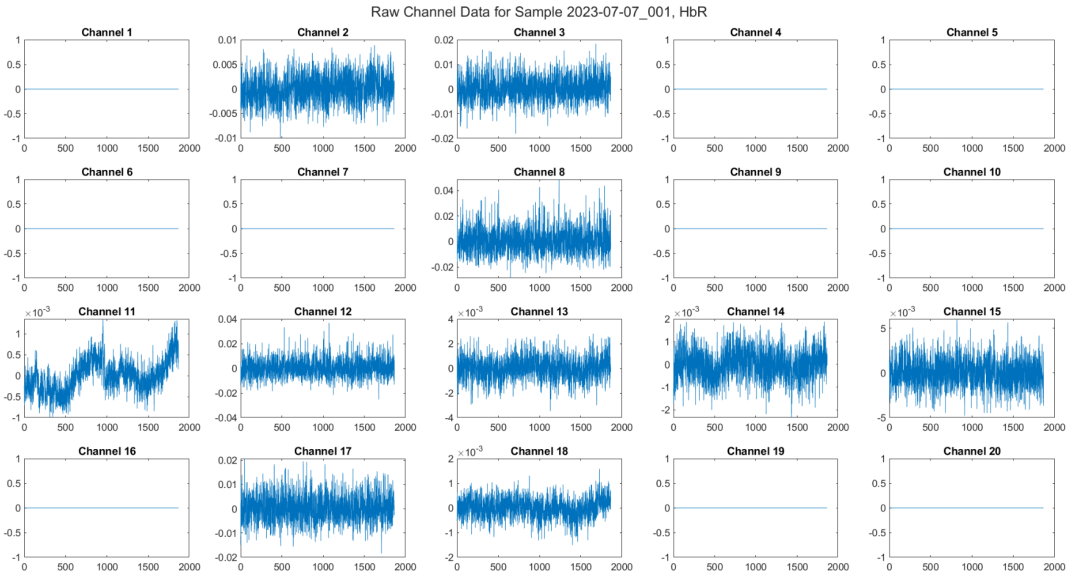

Figure 46: Raw data collection of sample 2023-07-07_001 for HbR levels measured in each channel

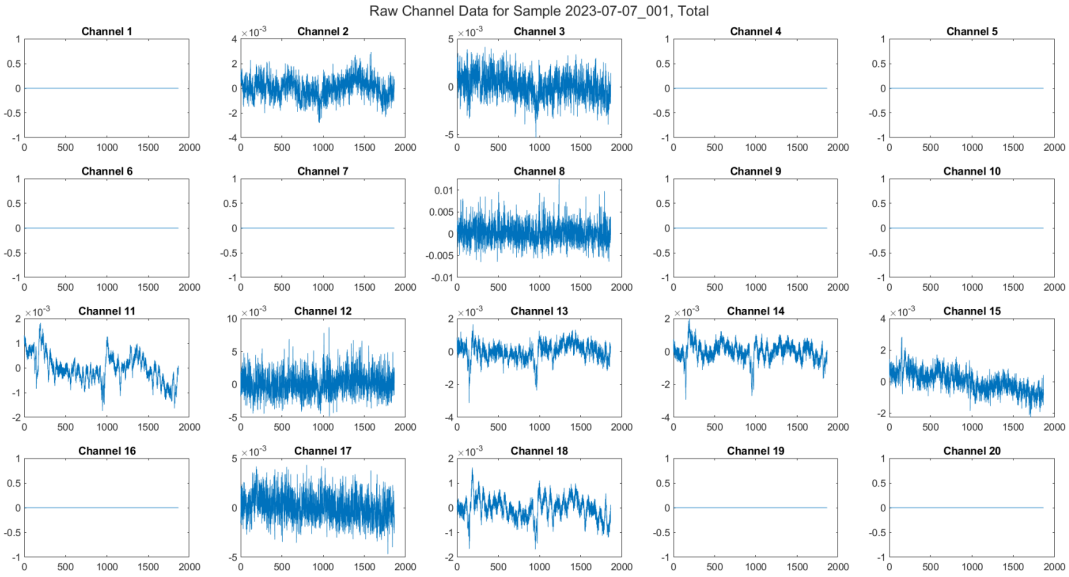

Figure 47: Raw data collection of sample 2023-07-07_001 for the total hemoglobin levels measured in each channel

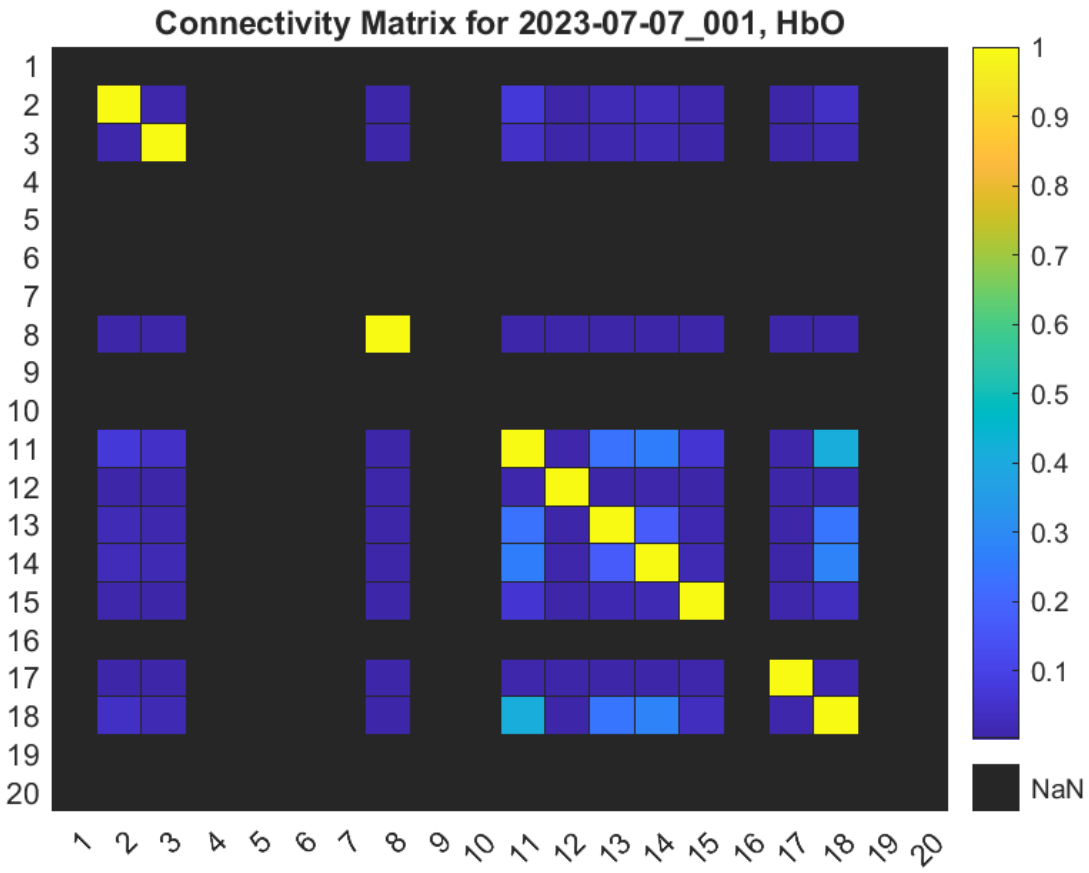

Figure 48: Connectivity matrix for HbO levels for sample 2023-07-07_001

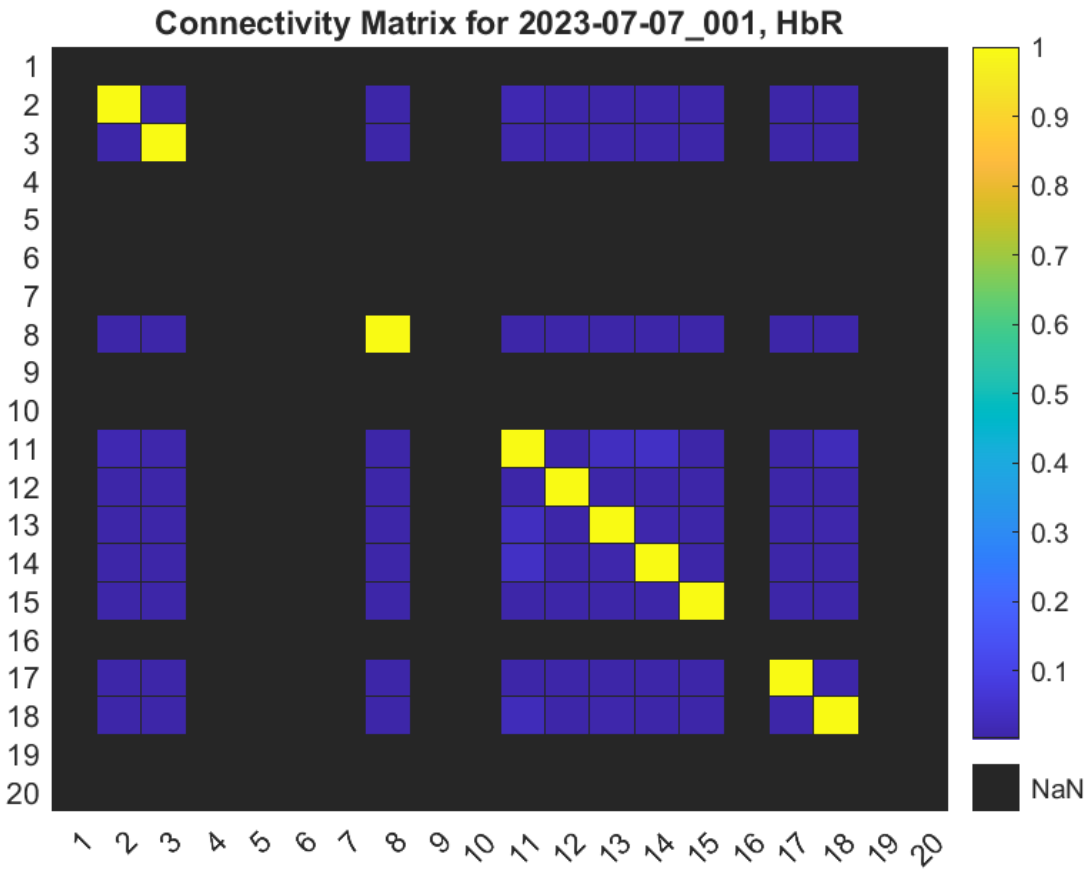

Figure 49: Connectivity matrix for HbR levels for sample 2023-07-07_001

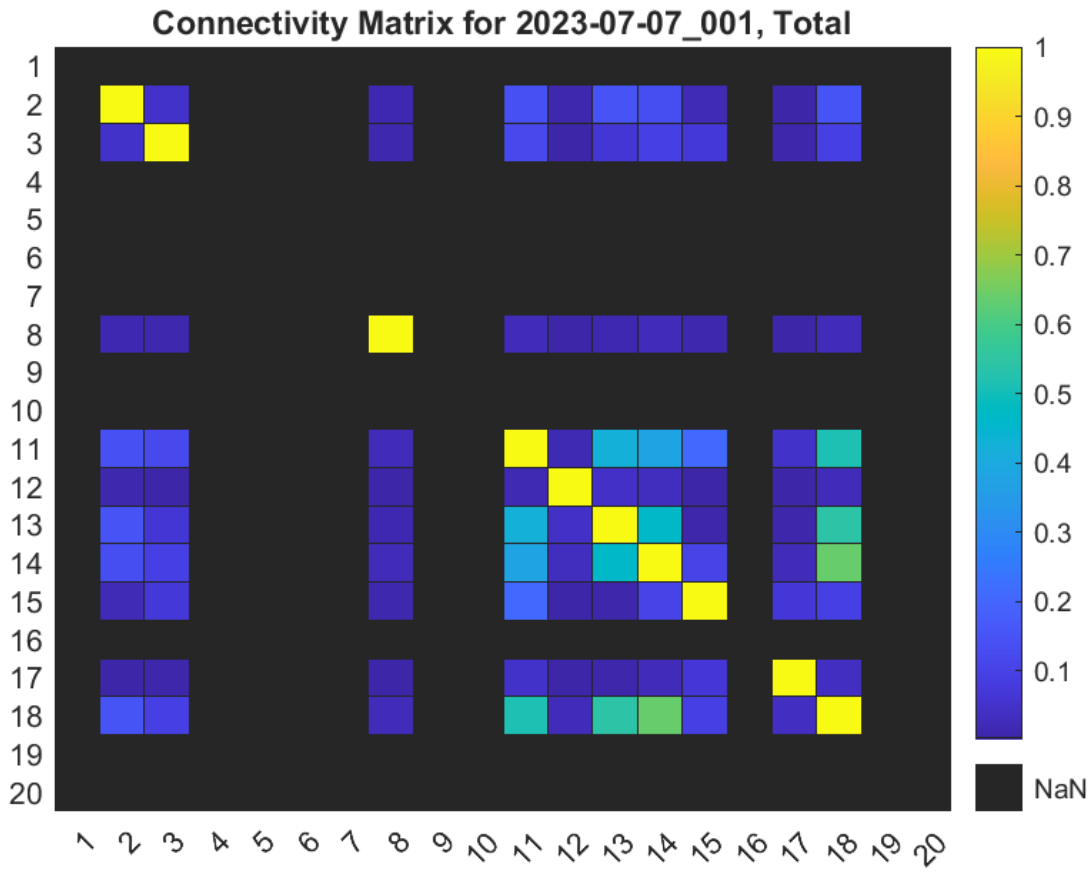

Figure 50: Connectivity matrix for total hemoglobin levels for sample 2023-07-07_001

7.6. Sample 2023-07-07_002

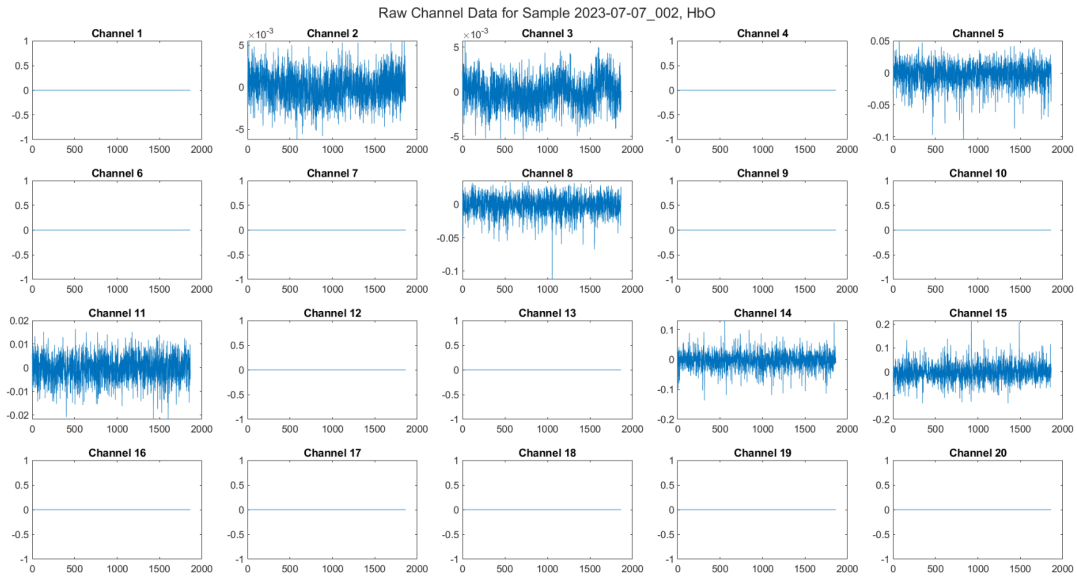

Figure 51: Raw data collection of sample 2023-07-07_002 for HbO levels measured in each channel

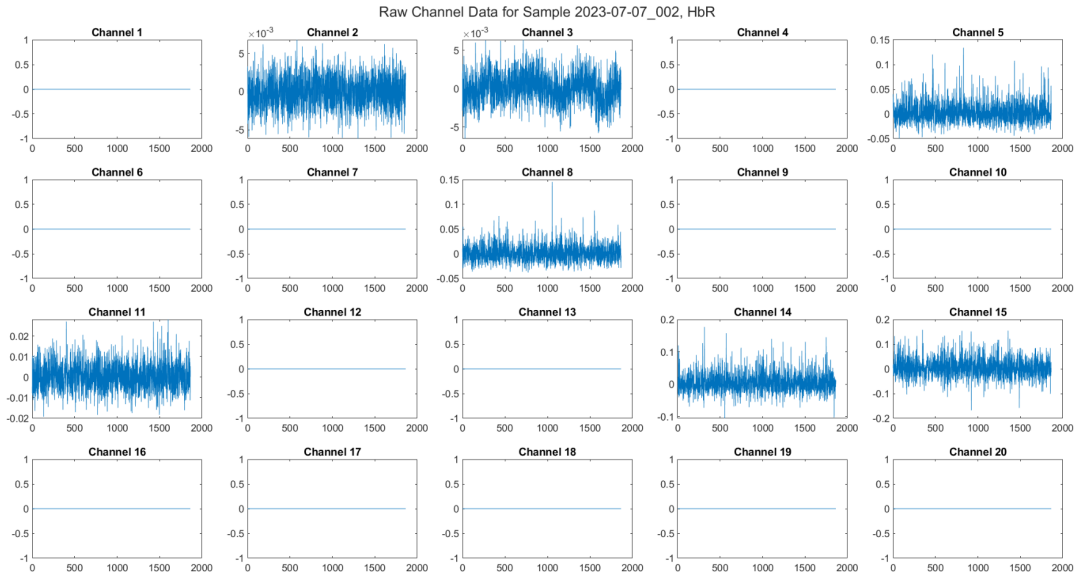

Figure 52: Raw data collection of sample 2023-07-07_002 for HbR levels measured in each channel

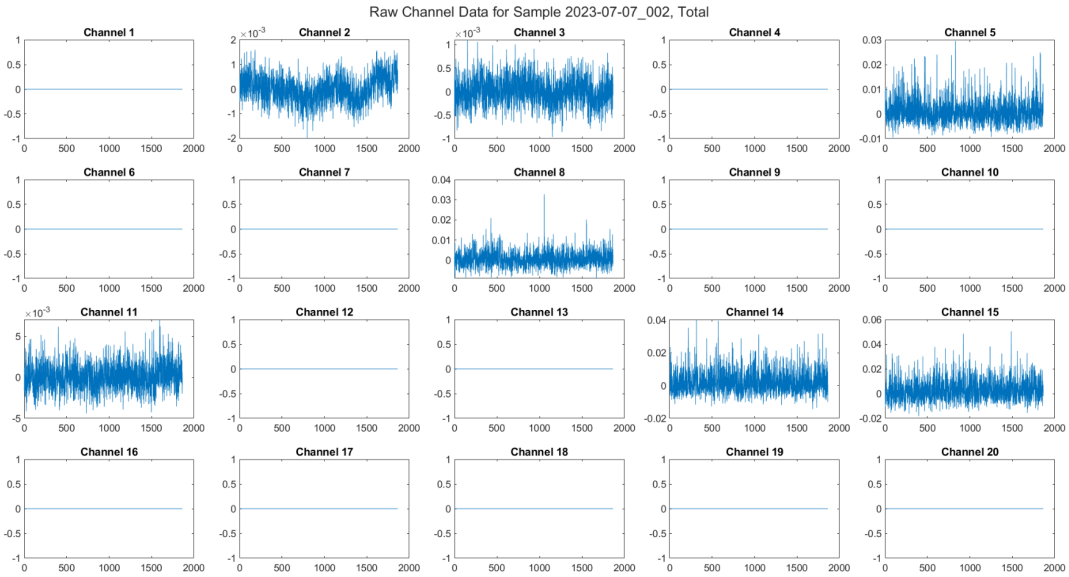

Figure 53: Raw data collection of sample 2023-07-07_002 for the total hemoglobin levels measured in each channel

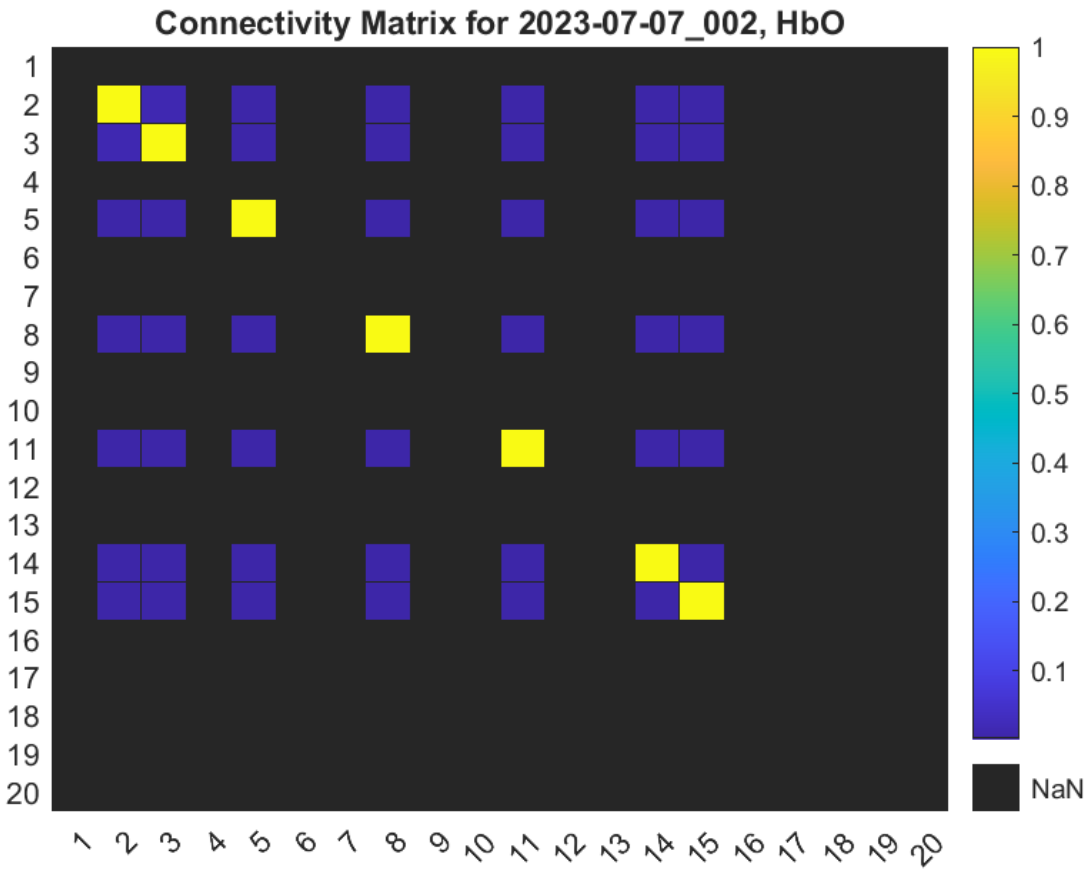

Figure 54: Connectivity matrix for HbO levels for sample 2023-07-07_002

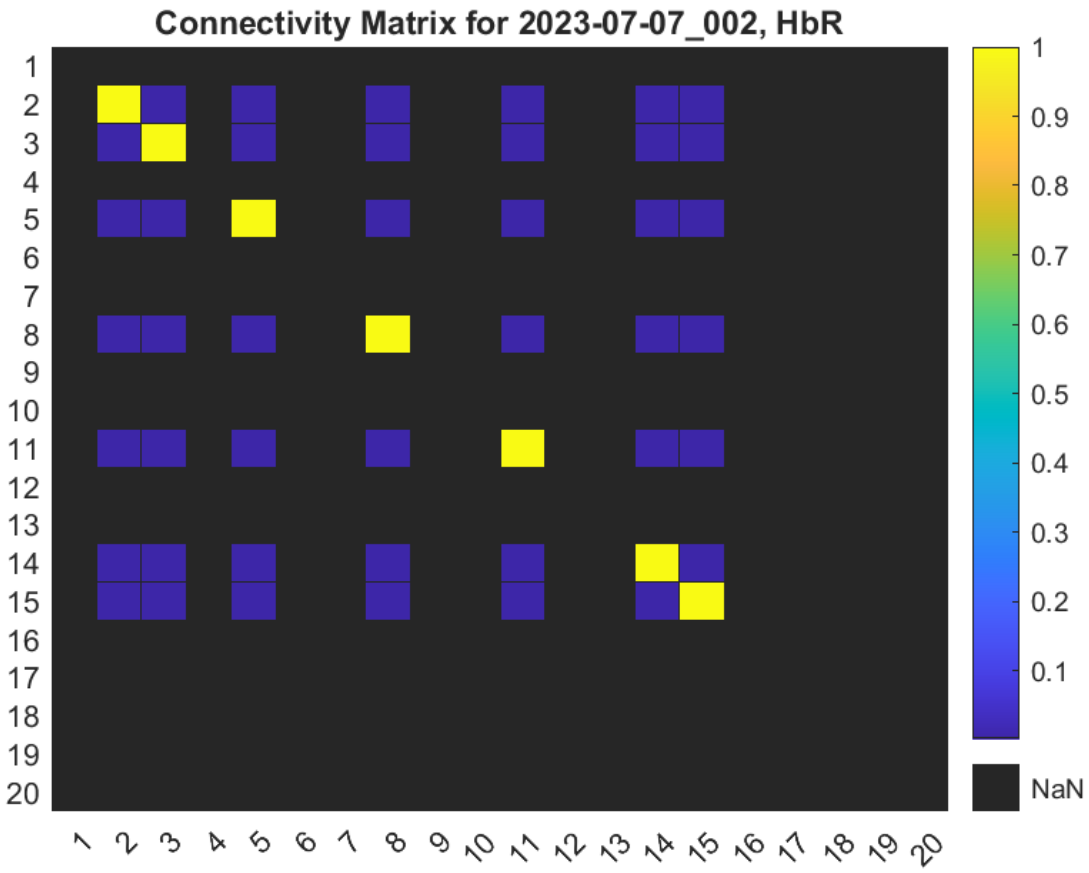

Figure 55: Connectivity matrix for HbR levels for sample 2023-07-07_002

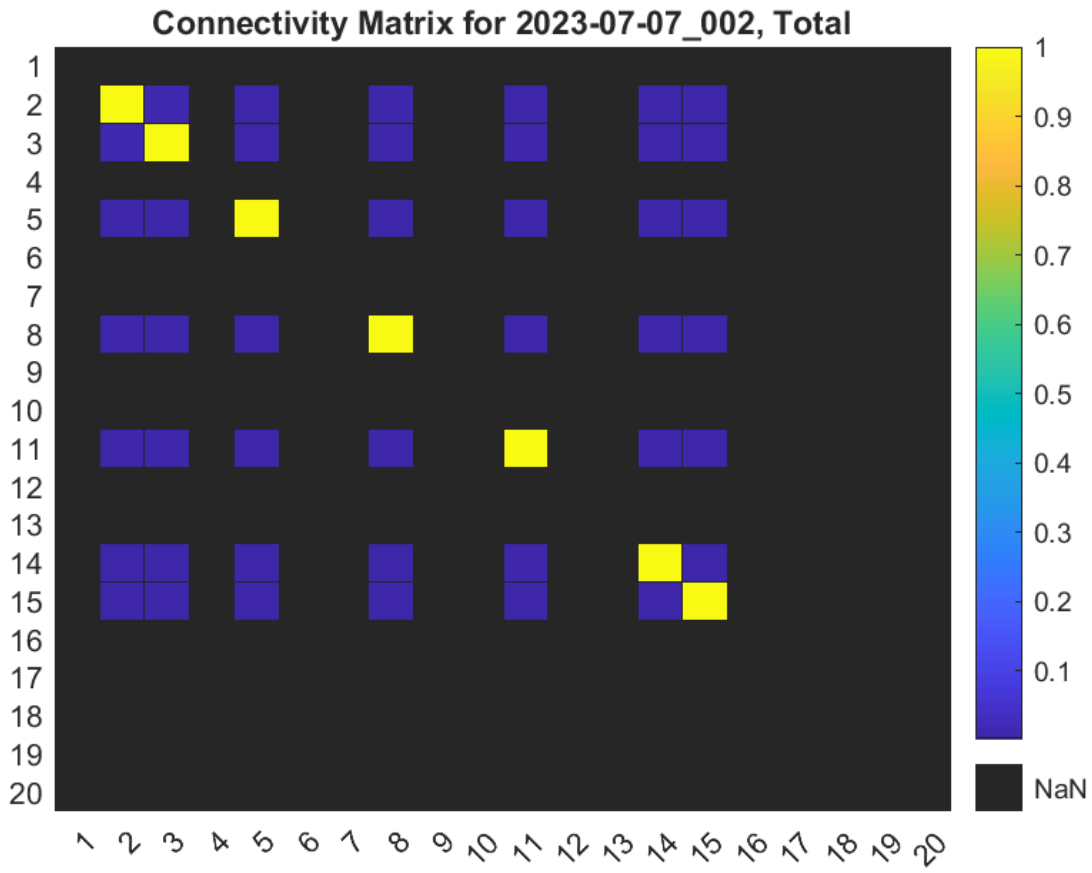

Figure 56: Connectivity matrix for total hemoglobin levels for sample 2023-07-07_002

7.7. Sample 2023-07-07_003

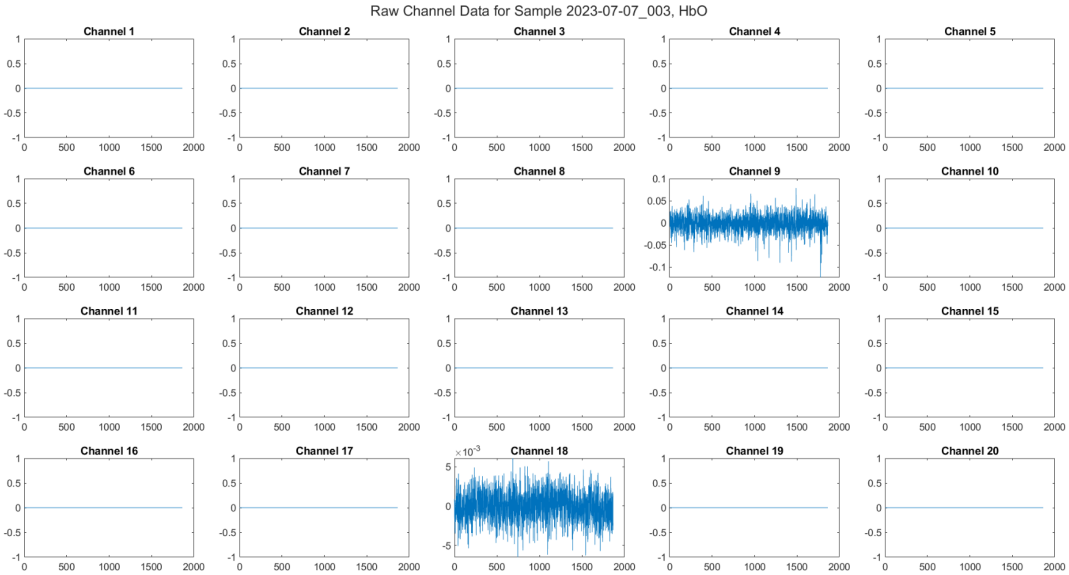

Figure 57: Raw data collection of sample 2023-07-07_003 for HbO levels measured in each channel

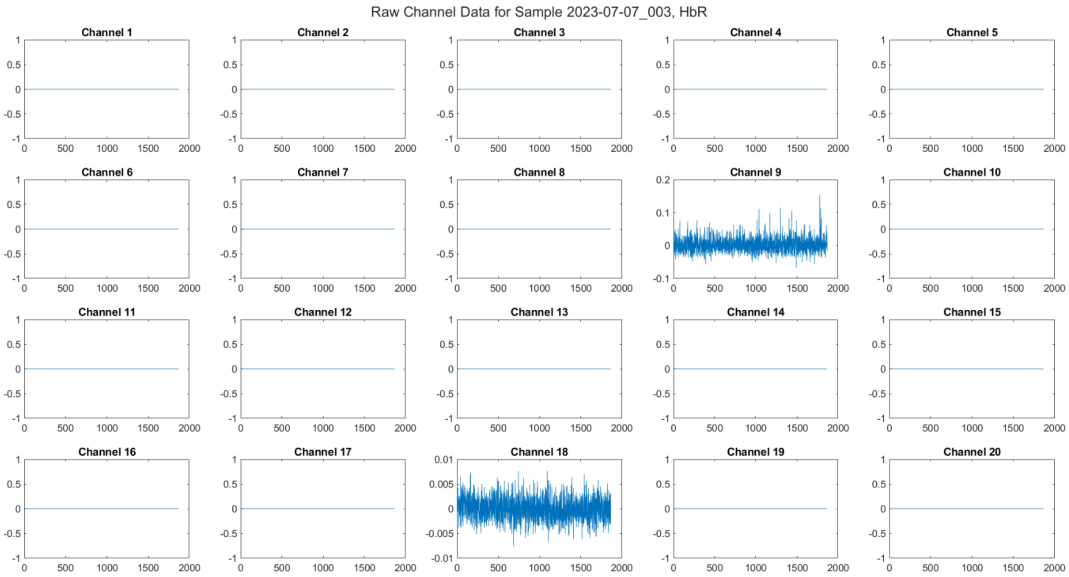

Figure 58: Raw data collection of sample 2023-07-07_003 for HbR levels measured in each channel

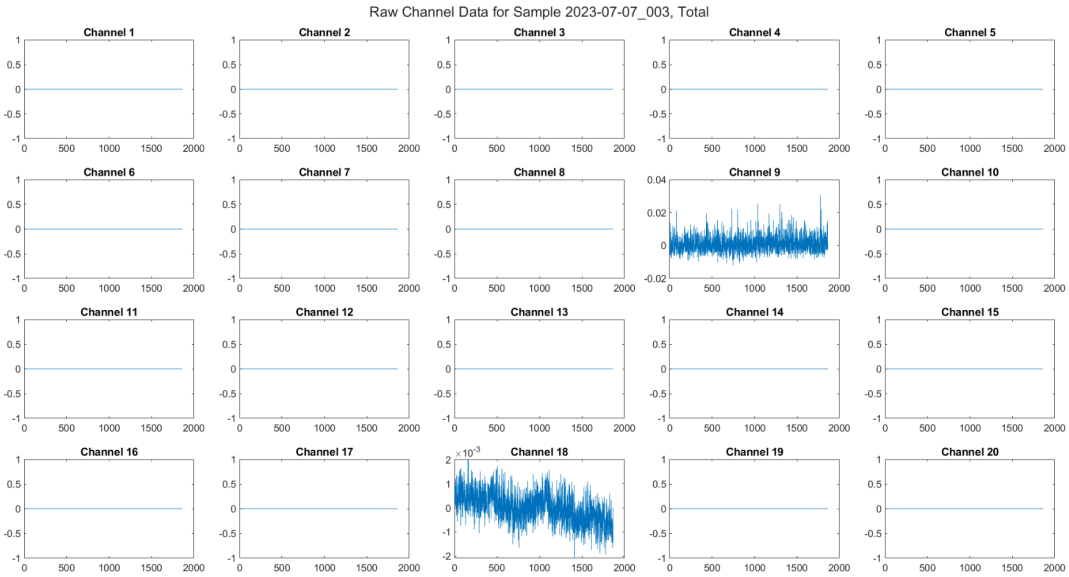

Figure 59: Raw data collection of sample 2023-07-07_003 for the total hemoglobin levels measured in each channel

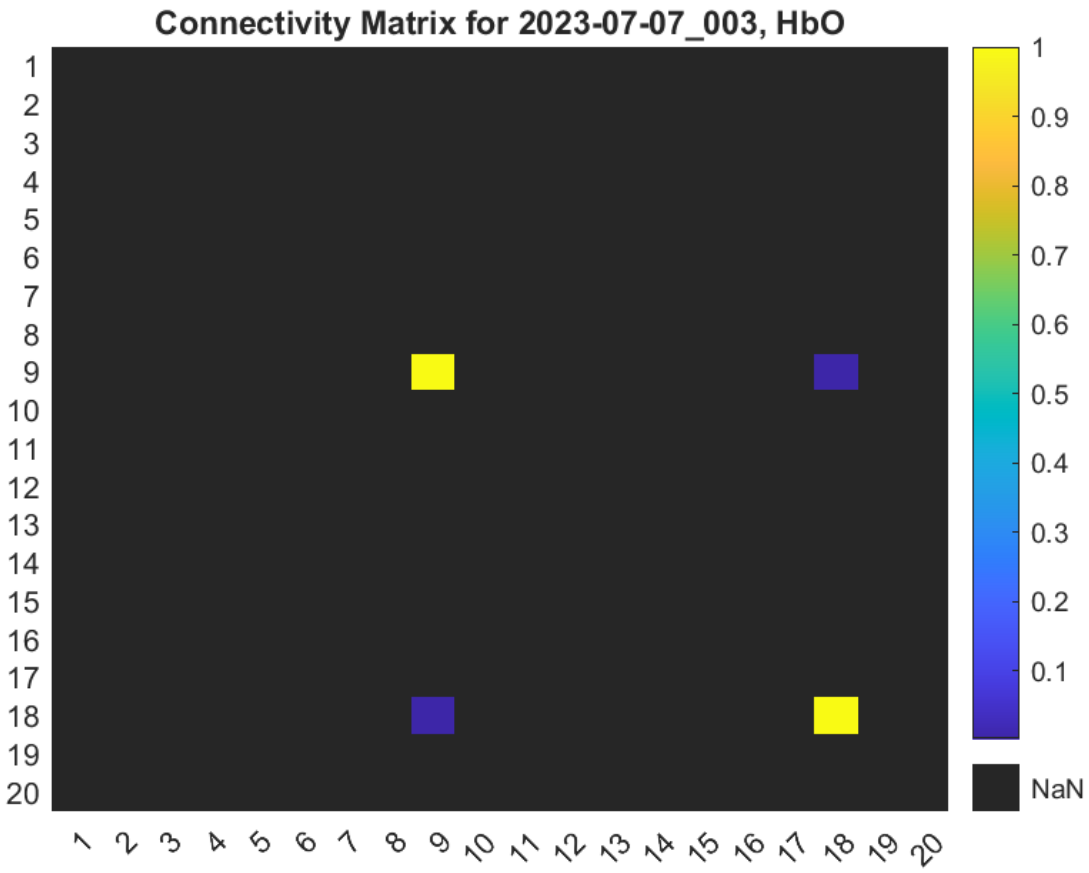

Figure 60: Connectivity matrix for HbO levels for sample 2023-07-07_003

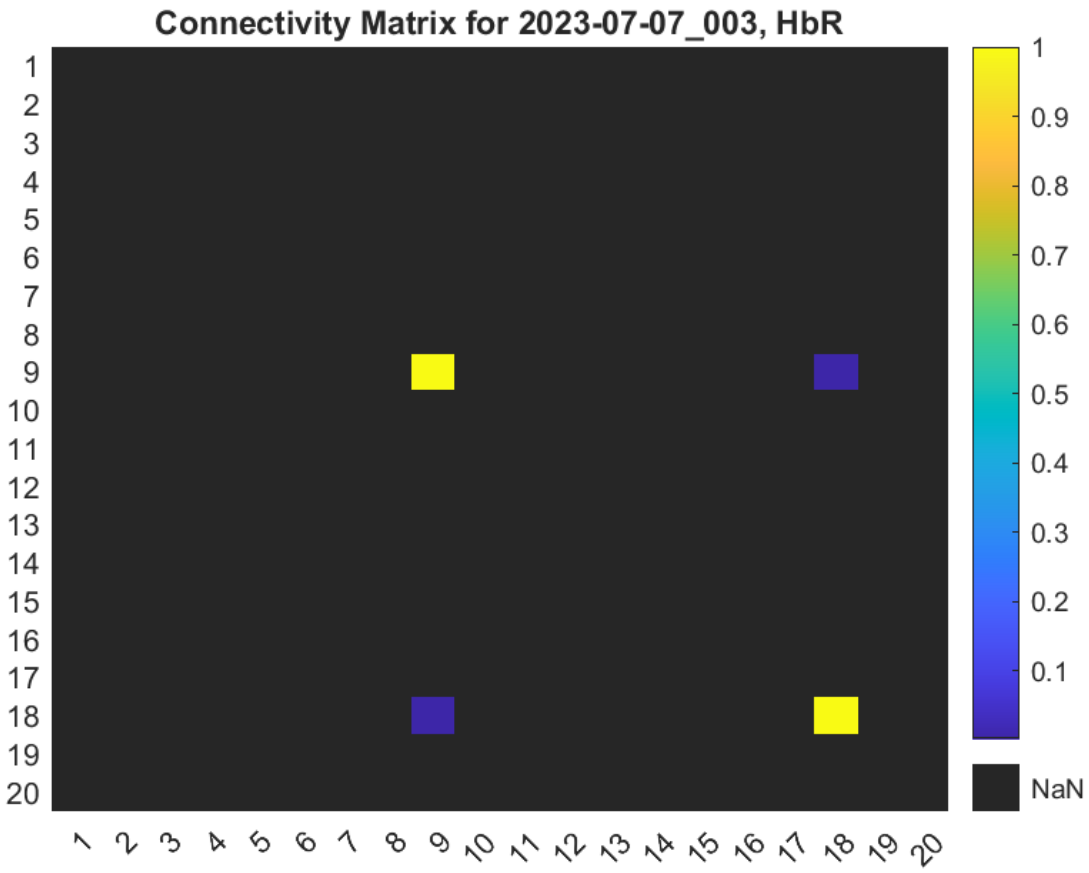

Figure 61: Connectivity matrix for HbR levels for sample 2023-07-07_003

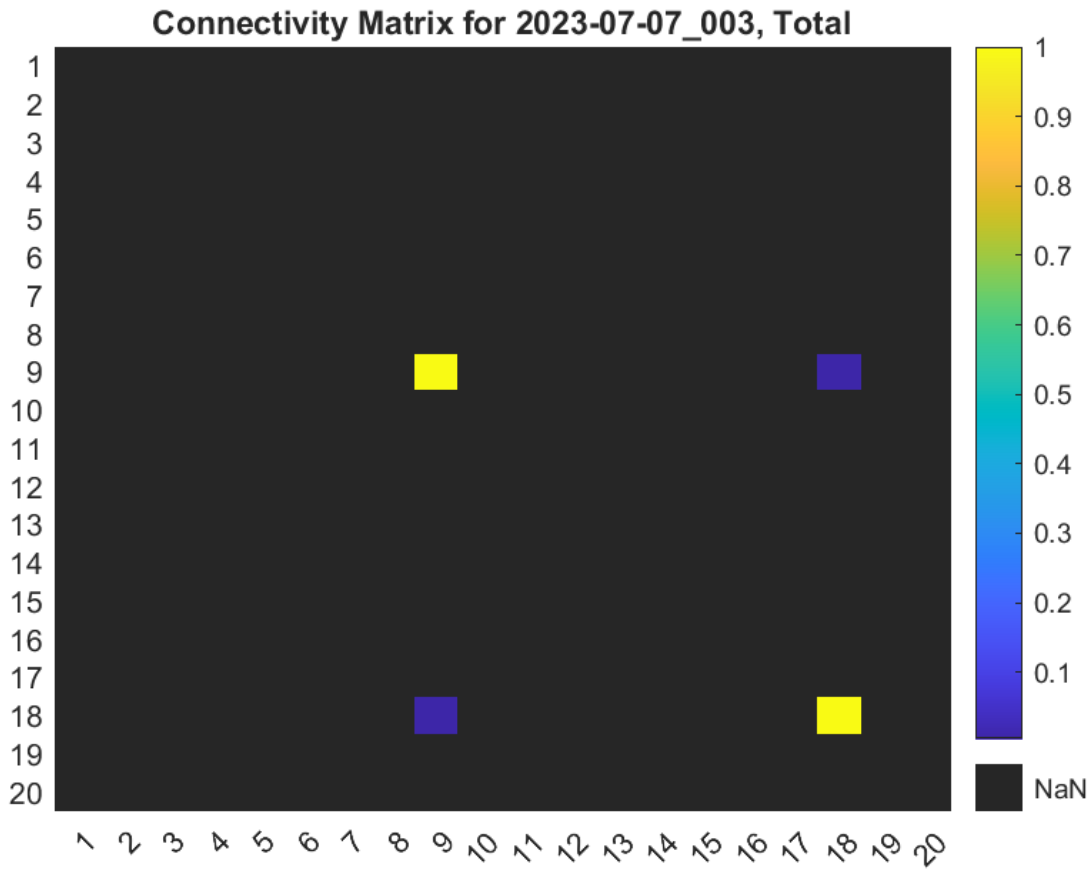

Figure 62: Connectivity matrix for total hemoglobin levels for sample 2023-07-07_003